Aalto-yliopisto
Aalto-universitetet
Aalto University

Master's Program in Chemical, Biochemical and Materials Engineering

Nanostructured Carbon from Biomass as a Catalyst for Energy Conversion Devices

---

Daria Osipova

Master's Thesis

2021

Aalto-yliopisto
Aalto-universitetet
Aalto University

Author Daria Osipova

Title of thesis Nanostructured carbon from biomass as a catalyst for energy conversion devices

Program Chemical, Biochemical and Materials Engineering

Major Functional Materials

Thesis supervisor Prof. Orlando Rojas

Thesis advisor Dr. Maryam Borghei

Date 16.02.2021 **Number of pages** 77 + 5 **Language** English

Abstract

The growth in demand for CO_2 free energy sources stimulates the development of more metal-air batteries (MABs) and sustainable catalyst alternatives from renewable or waste resources. In this project some abattoir wastes were applied to obtain porous carbon-based bifunctional electrocatalysts for the MABs. The porous carbon structure obtained from bones were functionalised with transition metals to improve electrocatalyst activities toward oxygen reduction reaction (ORR) and oxygen evolution reaction (OER), occurring in rechargeable MAB cathodes. The obtained electrocatalysts provide a more economical and sustainable alternative for commercially used catalysts proceeding from platinum on carbon black (Pt-C).

Catalysts synthesised from bone decorated with transition metals (Fe, Co) could demonstrate eminent ORR and OER activity. Specifically, ORR attained a 4 electron-transfer similar to Pt-C with more positive onset potential (0.92 vs 0.82, NHE). For the OER, better performance was observed with an onset potential of

0.38 V (NHE) compared to 1.48 V (NHE). Researching the production of catalyst form animal waste resulted in the following discoveries: (1) the surface morphology of the catalyst does not show an effect neither on ORR nor on OER; (2) transitional metals improve electrocatalytic activity synergistically; (3) secondary pyrolysis positively affects the catalyst performance.

Keywords Porous carbon, biomass conversion, bifunctional electrocatalyst, ORR, OER, nitrogen-doped carbon, transition metals.

Preface

This thesis was written to inspire future research on energy storage solutions. We can explore materials on multiple levels from nuclear to global observing the connection between the technology and its affect us on a daily basis. Across various societies, the absence of a consensus between them and notwithstanding an inherent desire to compete prevents these societies from slowing down the decay of conditions on Earth that are comfortable for us. The ways we source energy must change.

For a battery, autonomous performance may mean power from renewable and easily accessible resources like air, water, or plants. In this project I develop a catalyst by exploring the narrow part of a battery as a concept. Critically, the improvement of the catalyst as a physical part of this concept can improve the life-cycle of a battery, its weight, and its ability to quickly charge and recharge, which favours its use in households and vehicles.

By studying a material and exploring its qualities in different conditions, there is a prospect to find the satisfactory combination of required qualities.

This research was funded by European Research Council BioELCell. I would also like to acknowledge the Magnus Ehrnrooth foundation for the grant to purchase the equipment for this project. I want to thank Dr Maryam Borghei, Prof Orlando Rojas and the BicMat group for inspiration, encouragement, and most importantly, knowledge sharing. Additionally, support from Prof Tanja Kallio and valuable contributions from Dr Seyedabolfazl Mousavi made the exploration of electrochemistry possible. Finally, I want to thank Dramaturg, David Robertson for playing with me among the stars.

Helsinki January 2021

Daria Osipova

Symbols and abbreviations

A	electrode area, cm^2
C	analyte concentration, mol/cm^3
D	diffusion coefficient, cm^2/s
$\mathbf{E_o}$	standard potential of a redox reaction, V
$\mathbf{E_{1/2}}$	half potential, V
$\mathbf{E_{pa}}$	peak anodic potential, V
$\mathbf{E_{pc}}$	peak cathodic potential, V
F	Faraday constant, V
$\boldsymbol{I_L}$	Levich current, A
n	number of electrons transferred
$\boldsymbol{\upsilon}$	kinematic viscosity, cm^2/s
x	oxidation number
$\boldsymbol{\omega}$	angular rotation rate of the electrode, rad/s

avg	Average
BET	Brunner-Emmett-Teller
CV	Cyclic voltammetry
EIS-RU	Electrochemical impedance spectroscopy – uncompensated resistance
GDE	Gas diffusion electrode
L	From the Finnish word Luu: Bone
LSV	Linear sweep voltammetry

M	Metal
MAB	Metal-air battery
NHE	Normal hydrogen electrode
OER	Oxygen evolution reaction
ORR	Oxygen reduction reaction
Pt-C	20% Pt on Vulcan
RDE	Rotation disc electrode
RRDE	Rotation ring disc electrode
rsd	Relative standard deviation
sd	Standard deviation
SEM	Scanning electron microscope
TEM	Transmission electron microscope
V	From the Finnish word Veri: Blood
XPS	X-ray photoelectron spectroscopy

Contents

1. Introduction

This discussion will focus on carbon-based catalysts for energy storage and conversion solutions. Energy storage solutions are versatile systems with multiple components, and catalysts are one of them. Supporting global trends, special consideration in this project is given to sustainability. Electrocatalysts are utilised in areas that are beneficial for the environment, at the same time, production materials and methods correlate to safety requirements. The renewable precursor materials are developed from a production waste, that is recycled to become the carbon base of the catalyst. The choice of additional materials was guided by a cost-effectiveness analysis. Hazardous materials were avoided during the catalyst development. The importance of the avoidance is underlined in this chapter.

1.1. Global trends

The constant struggle for the reduction of fossil fuel resources draw more focus toward alternative energy conversion/storage technologies. The biggest challenge relates to on those responsible for the most CO_2 emissions, i.e. coal and mining industries, transportation. Programs striving for zero-emissions affect many powerplants (*4 Charts Explain Greenhouse Gas Emissions by Countries and Sectors | World Resources Institute*, n.d.). In the next three decades, some regions are aiming to achieve zero-net emissions (Hausker, 2019). All these actions involve electrification and require improvement in electricity storage devices.

Current dynamics in world politics also affect the energy storage market. With a change of political leadership in the US stagnation in green activity might end. The policies of Republicans did not support the country's sustainable development that hugely affects global environmental issues. Now, however, the new government supposedly will develop renewable energy initiatives. Nevertheless, forced rapid changes can always have consequences on the economy. As a consequence of the achievement of zero carbon emissions by 2050, an economical fall-out is feared by some (Mastini et al., 2021). On the other hand, a rapid transition might lead to opposite results provoked by a slowing of technological development, investments shift, and socio-political consequences.

Moreover, the clean energy market has experienced growth due to the global pandemic caused by COVID-19 (*Energy Investing Exploring Risk and Return in the Capital Markets - CCFI, IEA Report - v2 June 2020.Pdf | Powered by Box*, n.d.). Positive yields were experienced in the UK, USA, and Europe as a result of their investment in the renewable energy industry (*Just How Good An Investment Is Renewable Energy? New Study Reveals All*, n.d.). But neither could be said about the fossil fuel industry, which during the pandemic experienced heavy losses in both investments and consumers. In this way, oil prices dropped to negative values during April 2020 due to global instability and demand reduction (see Figure 1).

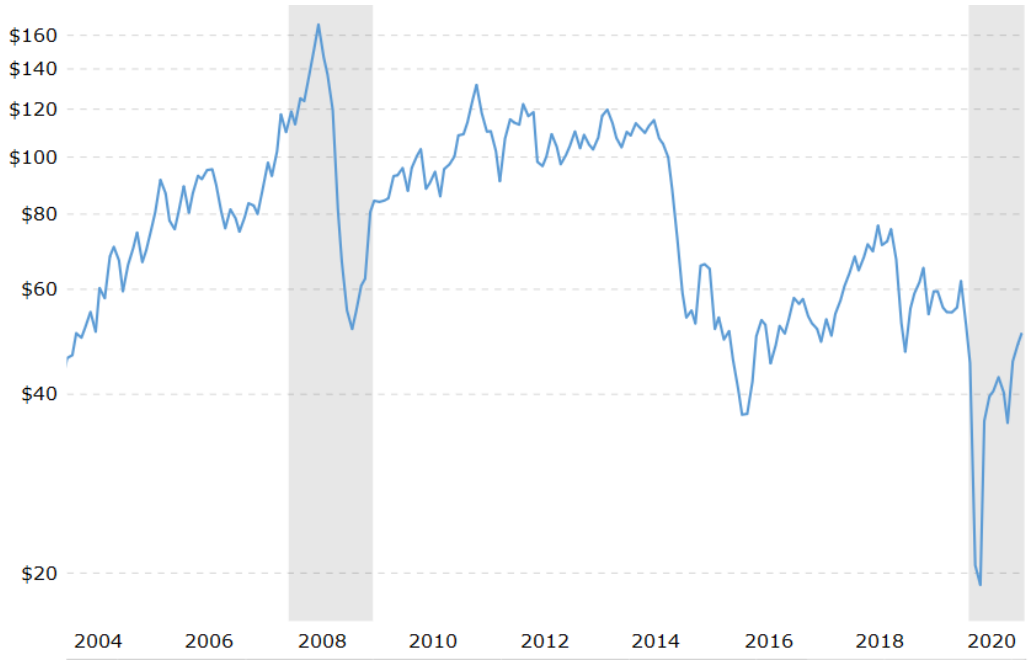

Figure 1 Crude Oil Prices (Macrotrends LLC).

Concerning the energy storage industry, leading companies' stocks jumped over the beginning of 2021. But the turbulence on the market is possible to continue. Director of the Centre for Climate Finance and Investment at Imperial College London Charles Donovan said: "The conventional wisdom says that investing in fossil fuels is more profitable than investing in renewable power. The conventional wisdom is wrong." There are multiple reasons for the lack of sufficient investments into green energy as opposed to fossil fuels. Conservatism could be listed as one of them. Uncertainty concerning the development of energy storage solutions is likewise unconducive to investment.

Furthermore, the returns on investment are low due to low liquidity of the developing market. The zero-emission pacts add additional pressure on the investors. According to the International Renewable Energy Agency, to cope with new emission standards, countries governments are faced with doubling have to double their efforts toward long-term sustainable development investment. Such requirements might diverge governments out of environmental deals. The future of an industry depends on the investments it receives. Apart from these external factors, properties of a product play an essential role in its position on the market.

At the time of writing, the Norwegian Road Federation (OFV) reports that battery electric vehicles in the Nordic countries constituted 54.3% of bought cars during 2020. The most significant global market share constitutes lithium-ion and lead-acid based batteries. Due to environmental concerns, hazards related to hydrogen accumulation which causes explosions and combustion, instability caused by overcharge, current peaks, and ageing better alternatives might replace lithium-ion and lead-acid based batteries. Notably, both weight and the ability to withstand various external conditions are also valuable factors concerning the development of energy storage solutions, which are conducive to investment.

A fuel cell, supercapacitor, or a MAB can be a source of power for an electric or hybrid electric vehicle. Development and improvement of such energy sources can make the electric vehicles a cheaper alternative to an internal combustion engine vehicle. In the last decade, the price for vehicle batteries decreased by 87%. (*Battery Prices Are Falling, Which Is Good News for EVs - Marketplace*, n.d.). Still, the electrode price constitutes around 50% of an energy device.

The cathode electrode high price arises from use of precious and semi-precious materials, which can provide enhanced electrocatalytic properties. The aim of developing a cathode catalyst is to reduce cost with the application of more accessible materials. The higher performance can be achieved by fine-tuning a material structure. The structure of a catalyst usually consists of a carbon support with inclusion of other materials promoting energy transfer abilities.

Carbon materials, especially functionalised nanostructured carbon, can be applied in all types of batteries and supercapacitors as a catalyst. By developing new catalytic material, it is crucial to take responsibility for every product life cycle stage. Materials, production methods, and properties must be sustainable. This involves paying attention to the scarcity of renewable resources required, as a rapid demand to supply new environmentally friendly

energy resources might exhaust them. This project involves processes that ensure health and safety. For example, a departure from the use of strong acid and alkaline solutions not only in materials used in batteries but also in the production materials is recommended.

The source of materials is also important. Most global production and mining companies developed over the course of the past two centuries defined standards of health and safety in a different manner to present day standards. These former customs still remain in practice in some parts of the world. As will be discussed further, cobalt was used in the practical part of this project. The biggest developer of cobalt nowadays currently is the Democratic Republic of the Congo, (DRC). At this point in time, however, companies like Apple and Google are actively fighting the exploitation of child labour (see Figure 2) by cobalt mining companies in the DRC. This and similar facts must be taken into consideration when making an ethically responsible choice for materials. The cobalt used in the practical part of this project was not procured through child labour.

Figure 2 A child labour at Congo cobalt mines (Toxic Leaks: The Price We Could Pay for a Greener Future | Green Economy | The Guardian, n.d.).

Not only compliance with international standards but also a commitment to maximise positive environmental impact are strongly recommended as an important part of future catalyst's development. The circular economy is a developing economic concept that enhances the use of resources. With the thinking understanding that nothing is waste, any resource can be recycled with the possibility of modifications. In this way, a growing industry will be closer to reaching zero imprint conditions.

Presently, wastes to a significant extent are disposed of without further value addition. This is a terrible waste for humanity. Carbon materials are easily obtained from organic matter by supplying energy to produce them. Combustion, for instance, is the most common way to do this. Carbon materials are commonly produced from cellulosic materials, such as grass and wood. Sludge recycling through pyrolysis is another efficient carbon production method (G. Hu et al., 2017; Samanya et al., 2012). In this project, a less obvious source of waste was chosen: abattoir waste.

Abattoir waste management requires thoughtful consideration (Franke-Whittle & Insam, 2013) as it represents a source of diseases and poisoning. This issue is not well researched yet. Moreover, it lacks publicity. According to some estimations 1,605.403 ton of abattoir waste produced in a year (Tolera & Alemu, 2020). This could be refined into 111.25 ton/year of bio-fertiliser and 85,139 m^3/year of biogas.

As will be discussed further, animal waste's structure and chemical composition make it an attractive source material for carbon catalyst production. In particular, porosity, the interconnection of aromatic polymers with mineral perovskite structures, and high carbon content are prerequisites for a quality catalyst.

1.2. Catalysts

Catalysts are used to change chemical reactions speed while staying intact. In this project, functionalised carbon will be investigated as a heterogeneous positive catalyst. In a solid-state activated carbon can interact on an interface with liquid and gas to produce energy. It can be used in applications when a catalyst is irreplaceable, for example, in batteries or applications, where it can benefit existing solutions, such as tissue engineering. For the sake of the present practical research, the focus will be on energy conversion applications.

To be an effective catalyst, a material should be able to reduce the reaction's activation energy. By increasing the reactants' activation energy, a catalyst allows them to easier reach the reaction activation energy easier. Some reactions will not proceed at all without a catalyst. A reaction will proceed without a catalyst only if the products are more stable than the reactants.

A catalyst interacts with one of the reactants to chemically or physically affect its properties. The stability and mechanical properties of a catalyst is a prerequisite. A catalyst support

composed form sp2 hybridized carbon materials has a trubostratic structure. Symmetricity of the hexagonal rings due to resonance and presence of double and triple bonds increases stability and reactivity.

With the addition of high temperatures or the addition of a catalyst, the hexagonal rings might open. But instead of an addition reaction, the resonance stability of the ring causes another molecule to replace a carbon. And in the presence of other compounds, the substitution reaction might take place. In this way, the carbon can be doped.

On the example of benzene as the most stable aromatic structure, the resonance stability can be explained. As benzene is a planar molecule, the overlap of all sizes carbon p-orbitals results in three bonding and three antibonding orbitals. The phases of the six orbitals overlap to form six bonding orbitals each for a pair of electrons. As all bonding orbitals are filled, a chemically and thermally stable closed-shell is formed.

The electron transfer abilities of a carbon material are essential for catalytical applications. And its aromatic structure embraces the speed of electron transfer. Electron transfer was explored in the research of vibrational wavepackets and was found to be ultrafast (Rafiq et al., 2020). The high-frequency multidirectional vibrations cause rapid charge separation through exciton formation. Ultrafast emission microscopy allows for the detection of extra energy generated to stimulate the reaction rate of the transformation from reactant to product. The analysed samples had structure represented on the Figure 3, that reminds the structure of the developed in this thesis catalyst. The vibrational wavepackets are, in a way, an interplay between electron transfer effects and low-frequency vibrations. Carbon materials might exhibit the formation of vibrational wavepackets due to the structure and possible doping. Developments in this area can improve understanding of catalysts.

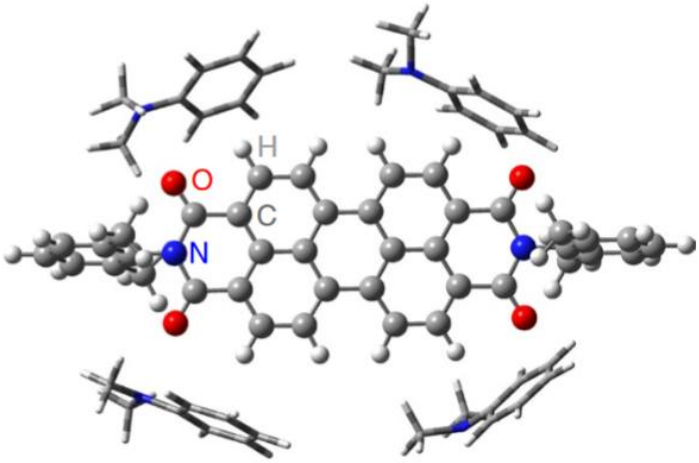

Figure 3 Chemical structure of the electron donor and acceptor (Rafiq et al., 2020).

A carbon catalyst can rarely outperform commercial products on its own. The addition of electron donors such as Pt into a carbon structure activates the reactants without changing them. Commercially used catalysts have to be reconsidered due to their high price and scarcity. By adjusting the chemical and structural properties of the carbon materials a Pt-free catalyst can be developed. One way to improve catalytic activity is to introduce nanoparticles into the carbon structure. In this project doping is used to incorporate transitional metals in the carbon support.

By introducing transitional metals within a carbon material structure, more active sites for electron transfer are formed. Adsorption energies of active sites and reacting species related to each other through a Volcano plot (H. F. Wang et al., 2018). Only at a particular relation of adsorption energies, the optimal electron transfer can occur. Catalytic properties can be adjusted through an introduction of transitional metals to assist desired reactions. Accordingly, the electrocatalysis can be anion or cation regulated.

Dependence of electroactivity on molecular configuration can be shown on the example of perovskite structures (see Figure 4). The arrangement of different atoms allows efficient multielectron oxidation/reduction (B. Q. Li et al., 2017).

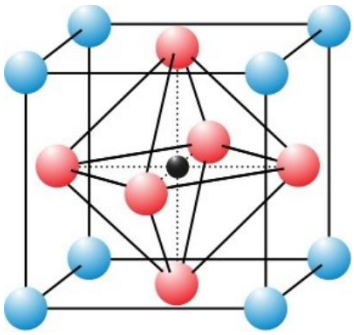

Figure 4 Perovskite structure (*File:Perovskite ABO3.Jpg - Wikimedia Commons*, n.d.).

Not only the nanostructure, but the microstructure of a carbon material affects its catalytic activity. The surface area is crucial for the catalyst as the reactions happen at the interface. The reactant interaction with the active sites and the possibility to functionalise the surface depend on the area of the catalyst's surface and the carbon's structure accessibility for liquid and gas.

1.3. Research questions and objectives

This project is aimed at the development of a porous heteroatom doped carbon catalyst. The carbon catalyst is to be developed from animal waste, which is an accessible low-cost renewable resource. The objective is to develop synthesis procedures to obtain materials with electrocatalytic activity. Specifically, electrocatalytic activity toward ORR and OER is the main objective and will be compared with commercial benchmark (20% Pt on Vulcan, Pt-C).

The opportunity to create value added products from waste can help industries to improve their environmental achievements. To improve electrocatalytic activities, further addition of catalytic metals including Co and Fe is considered, and the synthesis procedures and their effects is discussed.

1.4. Structure of the thesis

This thesis consists of five main parts. The introduction is followed by a technical review. The technical review contains a description of MABs and a catalyst within them. The main

electrochemical reactions take place at the surface of the presented catalyst. Moreover, precursor materials and the ways to develop a new catalyst are described.

A materials and methods section introduces the techniques used for carbon catalyst synthesis and characterisation. Physical and electrochemical methods of analysis are described there.

A results section explores properties that are important for an electrocatalyst performance. The relation of physical to electrochemical parameters is discussed. Moreover, effects of different synthesis methods are compared on an example of the reactions specific to MABs.

The conclusions are drawn on how effective the synthesised catalyst is and what are the questions that can direct the further development of the project.

2. Technical review

Many industries rely on catalysts in chemical manufacturing, waste management, energy production, and conversion operations. All these operations are the basis for renewable energy technologies. Improvements in energy storage devices can accelerate remediation of global problems. Therefore, there is a need to develop carbon zero-emission energy storage recourses (Jie Zhang et al., 2019).

To provide sufficient solutions, the energy storage methods must be accessible and sustainable. Batteries that charge and recharge can meet the need for affordable energy solutions. Therefore, the price of the production and materials should be reduced. Nowadays, Pt is used as a catalyst at both anode and cathode of MABs (Jie Zhang et al., 2019). Replacement of such catalyst components with alternative cheaper, renewable materials will reduce the environmental impact.

The selection of a new material requires certain qualities to be met. The carbon catalysts performance is often inferior to carbon precious metals (e.g., Pt-C) hybrid catalysts. That is why a special consideration has to be given to the development of carbon catalysts properties and their compensation with the addition of non-precious materials to allow for commercialization.

The commercialization perspectives of a catalyst depend on degradation pathways and life-cycle of the material (Shao et al., 2019). Oxidation of carbon and the loss of metals are the most common reasons for the degradation and decay of electrochemical activity (Singh et al., 2019). Usually, the prevention of degradation and prolongation of the life cycle is required through careful research and analysis (Banham et al., 2015) (Martinez et al., 2018).

2.1. Metal-air batteries

The MAB market was estimated to be USD 1.01 billion in 2019. Growth is expected to reach 9% in the next six years, according to the Air Electrode Battery Market Analysis Report (*Air Electrode Battery Market Size | Industry Report, 2020-2027*, n.d.). MABs are emission free and their components can be produced from renewable resources (Jie Zhang et al., 2019). They can convert renewable resources into energy, which leads to a positive environmental impact. Moreover, MABs eliminate the need to store fuel. Due to the rapid

development of functional materials an interest in the possibilities of MABs has renewed. If power density and specific energy are to increase, MABs' production can be scaled up.

Originally known as small electronics power sources, MABs are aiming at the electric vehicles market presently. Métalectrique is MAL Research & Development limited company that claims to produce MABs that can power a car for a 1500-mile drive (*Home | Métalectrique*, n.d.).

2.1.1. Characteriastics of metal-air batteries

The batteries are compared by current density or output current; in other words, how much cell voltage can be generated. The difference comes from variations between electrode potentials of different electrochemical reactions. In MABs the reactions take place at a metal anode and an ambient air cathode. The structure of a zinc (Zn) -air battery can be seen in Figure 5. Ions are supplied by an electrolyte that can be liquid or solid (Ren et al., 2020) (Jung et al., 2014). An insulating separator is placed in the electrolyte. The metal anode and cathode materials can vary in MABs to be, for example, foam, fiber, sponge, or alloy, and metal-free carbon, spinel, perovskite, or metal-nitrogen-carbon (M-N-C), correspondingly. The common feature will be the gas diffusion electrode (GDE) that provides gas permeation and electrolyte support at the same time.

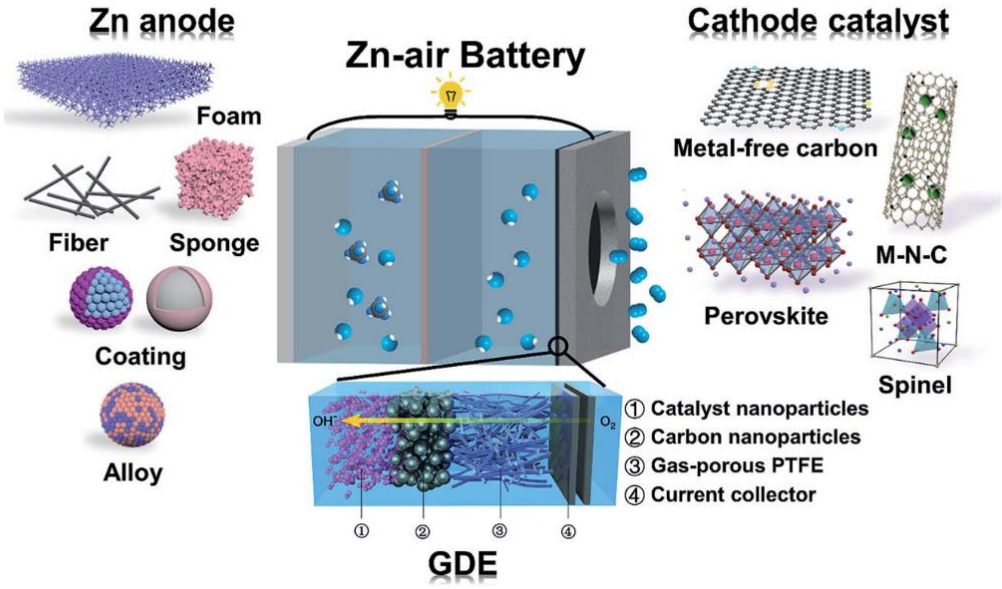

Figure 5 Structure of a metal (Zn) -air battery (Jie Zhang et al., 2019).

A MAB cathode thickness is approximately 0.5 mm. It consists of a gas diffusion layer and carbon catalyst layer separated by a microporous hydrophobic layer, which prevents the water molecules' passage in a liquid state. Water retains inside the catalyst to induce proton exchange. The catalyst hydrophilicity and presence of a conductive ionomer drive oxygen through it. The access to oxygen through the GDE results in the high specific capacity of MAB.

The metal anode oxidises during the discharge of a battery, supplying electrons to the cathode through an external circuit. Oxygen rescues at the cathode until electrons are supplied. The ability of the metals to oxidise vary, as well as the ability to reduce to the original state during a reverse reaction. Only certain metals can become an anode material for a MAB due to a proton-electron structure that is flexible in electron exchange. While only oxygen is considered in this report, other gases can be reactants in MABs.

Typical problems in MABs are associated with the stability and volatility of their components (X. Zhang et al., 2016). The instability might be caused by a formation of a reactive superoxide ion (Hartmann et al., 2013). The electrochemical activity dynamics also affect the performance and can be improved by a catalyst. The formation of dendrites is a common problem in different types of batteries. Their growth is caused by a rapid electron transfer between anode and cathode establishing contact between the circuit nodes with different voltages.

2.1.2. Reactions

The principle of electron transfer in rechargeable MABs is based on a reduction and an oxidation of oxygen from air. The electron is given up at the anode moving externally to the cathode, creating electron flow, and the current flows in the opposite direction (towards the anode). The electron configuration of a material is responsible for tendencies to lose or gain electrons. Equations 1 and 2 describe reactions that take place at the anode and cathode of a MAB (Dong & Wang, 2018).

Anode: $M \leftrightarrow M^{x+} + xe$ (1)

Cathode: $O_2 + xe + 2H_2O \leftrightarrow 4OH^-$ (2)

Where, M stands for a metal and x for its oxidation number. When a battery gives charge, metal ions leave the anode and oxygen is consumed at the cathode. The reverse reaction results in the production of oxygen and the re-plating of a metal on the anode surface. This is the bifunctionality principle of charge and discharge of a MAB. Consequently, oxygen reduction reaction (ORR) and the reverse oxygen evolution reaction (OER) are the governed by the catalytical activity of the cathode.

The most passive reactions are the in terms of standard potential are likely to occur spontaneously. In a MAB, the reduction of a metal-ion to a metal molecule is negative in potential and thus unlikely to happen by itself. Nevertheless, the reverse oxidation is very favourable due to reversion of the negative sign to a positive potential. Improvement of this mechanism will help to overcome the challenges in practical applications of bifunctional MABs and enhance their potential with carbon-based catalysts.

When these reactions take place, the catalyst provides active sites for the electron transfer. The state of the reaction at different sites will vary producing a pool of reactant and product molecules (see Figure 6) (Lao-atiman et al., 2019). The constitution of the catalyst, electrolyte and the air are represented schematically in Figure 6. A solid cathode surface is in contact with both gas (air) and liquid (electrolyte). The efficiency of ORR depends on the

interaction at the solid/gas/liquid interface. The porosity of a catalyst and GDE permits the increase of the interface area.

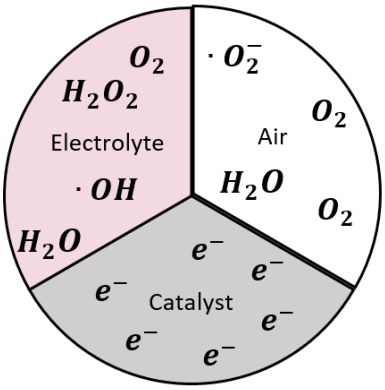

Figure 6 Gas/electrolyte/catalyst interface.

Different conditions produce different results as oxygen molecules will bind at various locations. The composition can increase the performance allowing the catalyst to compete for a good ORR and OER. For example, nitrogen-containing catalysts showed an increase in electroactivity due to their morphology, which, at the same time, affects the mechanism of the electron transport (Ni et al., 2012).

The crystal structure of a catalyst will affect the adsorption of oxygen on the surface. It can be bridge type, when both oxygen atoms are bonded with catalyst molecules, or an end type adsorption when only one oxygen atom is adsorbed. Hydrogen peroxide is more likely to be generated by bridge adsorbed oxygen, as each oxygen atom is equally attractive for hydrogen atoms. Protonation will reduce the bond with the catalyst, and H_2O_2 is generated. End adsorbed oxygen exposes only one atom to protonation, making the second atom inert. So, they are separated when two hydrogen atoms react, forming water.

The theoretical voltage of reactions is compared to the hydrogen potential, which is zero. ORR occurs at a cathode with 1.23 V and hydrogen oxidised at the anode giving anode potential 0 V (Ma et al., 2019). This potential difference is the cell voltage. The potential difference across the electrolyte causes the internal resistance. It is accounted with the potential difference.

When a MAB is charged, an electron conducted by carbon reduces an oxygen molecule, and a proton thermodynamically forms the water solution (see Equation 3). Water

molecules diffuse in hydrogen protons at a ratio 2.5 to 1. Consequently, the water molecules are responsible for transporting the protons from the membrane to the catalyst layer.

$$O_2 + 4H^+ + 4e^- \rightarrow 2\,H_2O \quad (3)$$

Electron transport is crucial for good electroactivity (Tao et al., 2020). There are two paths the ORR can proceed along: a four electrons reaction (see Equation 4) or two two-electron reactions (see Equations 5 and 6). The catalyst and the electrolyte govern the electron transfer during these reactions.

$$O_2 + H_2O + 4e^- \rightarrow 4OH^- \quad (4)$$

$$O_2 + H_2O + 2e^- \rightarrow HO_2{}^- + OH^- \quad (5)$$

$$HO_2{}^- + H_2O + 2e^- \rightarrow 3OH^- \quad (6)$$

During ORR hydrogen peroxide forms as an intermediate kinetic product. Reduction of oxygen to hydroxy peroxide (see Equation 7) determines the dynamics of the electroactivity of a material. The theoretical voltages of the reduction reactions are: a four electron four proton pathway, which reduces two water molecules at E=1.224 V vs. NHE, or a two electrons and two protons, which reduces a single molecule of hydrogen peroxide at E=0.695 V vs. NHE (Hartmann et al., 2013).

$$O_2 \xrightarrow{e^-} \cdot O_2^- \xrightarrow{e^-} H_2O_2 \xrightarrow{e^-} \cdot OH + OH \cdot \xrightarrow{e^-} 2H_2O \quad (7)$$

When the ORR is reversed, OER takes place at the cathode. As can be seen in the Equations 8-10 the reactants and products of the reaction can vary. In general, the process of water splitting into oxygen and hydrogen gases takes place (M. Li et al., 2020). Equation 8 shows how electrons transferred externally from the anode attach to hydrogen gas protons contained in a water molecule at the cathode surface.

$$4H_2O + 4e^- \rightarrow 2H_2 + 4OH^- \quad (8)$$

The electrons are released from the cathode and transferred to the anode in the electrolyte (see Equation 9). In this way, water splits and hydrogen gas evolves at the cathode and oxygen gas at the anode (see Equation 10). This electron-proton exchange is balanced in regard to the alkaline environment of an electrolyte.

$$4OH^- \rightarrow 2H_2 + 2H_2O + 4e^- \quad (9)$$

$$2OH^- + 2e^- \rightarrow O_2 \quad (10)$$

2.2. Electrode materials

2.2.1. Carbon materials from wastes

To produce a porous carbon catalyst from animal bones pyrolysis is used. Pyrolysis is a thermal treatment of materials in an inert atmosphere. The inert atmosphere prevents combustion, allowing decomposition of organic materials at elevated temperatures. On the one hand, the decomposition through pyrolysis is a waste management measure; on the other, it is a production of value-added components. Pyrolysis of animal derived wastes can be utilised to produce bio-oils. The yields of tar can be up to 30% (Isahak et al., 2012). However, the catalyst production requires quality char. Low heating rates and a high temperature of pyrolysis result in a crystalline structure of char. The use of animal waste as a precursor for the catalyst provides functionalisation with metals contained in bone and blood. This doping was shown to be more effective than doping with external sources by some researchers (Lv et al., 2019; Z. Zhang et al., 2019; Z. Zhao et al., 2019). Methods of carbon production derived from animal waste needs to be sustainable. Use of ammonia (Kang et al., 2019; F. Song et al., 2019) or acids must be reduced or illuminated during production (Isahak et al., 2012).

Recent developments in batteries not only utilise animal waste, but also get inspiration from it. The structure of a bone and its electrical properties can be mimicked to create a functional battery catalyst (Huang et al., 2011). Porous materials show high activity as a bifunctional cathode in a MAB (Niu et al., 2019). After pyrolysis the bones do not change their

mechanical properties significantly, while the electrical properties improve. Bones from different sources did not show variations in their char properties (Huang et al., 2011; Krzesińska & Majewska, 2015; H. Song et al., 2014).

There are various devices and methods for pyrolysis available, but generally, they can be categorized into three groups: conventional pyrolysis or carbonisation, fast pyrolysis, and flash pyrolysis. The parameters distinguishing these categories are temperature range, heating rate, particle size, and residue time. By and large, the heating rate is the defining criterion, with fast pyrolysis having temperature range from 10 to 200 °C/s, and flash pyrolysis higher than 1000 °C/s (Bridgwater, 2012). In fast and flash pyrolysis cases, the residue time is relatively short, and often the sample is placed in an already heated reactor.

Biomass pyrolytic processes follow some general principles regardless of the conditions. Primary pyrolysis is the degradation of initial components accompanied by the formation of pyrolytic products, while reactions that involve these products are called secondary pyrolysis. Pyrolytic products are char, which is a solid residue, and volatiles: condensable liquids called tar, and non-condensable. Charring is an exothermal process, while volatilization is endothermal (Bai et al., 2020; Zong et al., 2020).

An increase in a pyrolysis temperature leads to the formation of more gases (vis. more CO, H_2, but less CH_4, CO_2), the advance of the higher heating value of the gas phase, and less char and liquid (Couhert, Commandré, et al., 2009; Couhert, Commandre, et al., 2009). More liquid, less gas, and char will be produced with a higher heating rate (Asmadi et al., 2011; Xue et al., 2015). Both an intense evaporation of intermediate products as well as the depolymerization at higher heating rates can be attributed to this (Abnisa et al., 2013). Furthermore, gases released will affect the morphology, for instance, pore architecture. Also, it was shown that higher a heating rate is associated with fewer interactions among biomaterials (Long et al., 2016). During secondary pyrolysis, a cracking of liquid hydrocarbon causes gases formation, and a cracking of gaseous hydrocarbon results in H_2 formation (S. Zhao et al., 2018).

Not all products which formed during pyrolysis escape immediately. They can be trapped within the components or\and react with the components. Gaseous products trapped inside a biopolymer structure increase the vapor pressure. The higher vapor pressure stimulates polymerization reactions that lead to char formation and higher gas yield (Q. Liu et al., 2011). The polymerization reactions are favourable for a catalyst structure, due to it being more conductive.

Char properties like porosity and specific heat capacity are essential for the catalytic properties and interaction with other components, like metals during further pyrolysis. The char gasification and oxidation reactivity, which favors the interactions, are higher at lower pyrolysis temperatures. Also, the reactivity of char produced at high heating rates is increased. This is explained by higher porosity that results in a more significant surface area (J. Hu et al., 2019). The intrinsic reaction rate of char is dependent on the available char surface area. This latter is often assimilated to the BET (Brunaeur – Emma - Teller) surface area, which includes both external surfaces and inner pores' walls surfaces, and is generally measured using a nitrogen gas adsorption manometry. Chars produced from different components will have different porosity and shall not be judged by the solid particles' solely (Koschwanez & Reichert, 2013).

Biomasses contain cationic mineral components (e.g. alkali, alkaline earth metals), which vary depending on biomass type. They might be removed from samples before pyrolysis most commonly be washing; however, their residues will be still present to some extent. Ashes are formed by the minerals during pyrolysis and can act as catalysts (S. Wang et al., 2008; Yildiz et al., 2015). On the other hand, ashes formed by such compounds as, for example, silicon or phosphorus, can decrease the conversion rates of char (Strandberg et al., 2017). The presence of even 0.5 wt.% ash can change the composition and proportion of the pyrolytic products (J. Hu et al., 2019).

To understand the structure of the resulting char, that is used as a catalyst, the precursor material's composition must be studied. In this research animal bones and bovine blood were used. Below, the description of bone and blood constituents and morphology is presented.

Bones consist of different types of cells; each of them has its purpose and properties. For example, osteogenic cells can transform into osteoblasts, which is a bone matrix. This matrix consists of collagen and calcium-binding proteins. Osteogenic cells are responsible for bone growth. Stresses and strains are maintained by osteocytes, which are the mature cells, that do not divide because they are trapped in lacunae (Wippert et al., 2017). In Figure 7 can be seen the anatomy of a bone.

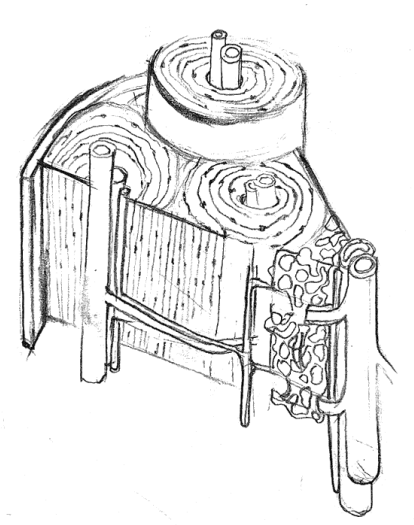

Figure 7 Bone structure.

The Figure 7compact (lamellar) bone consists of circumferential and interstitial lamellae, a Haversian system, canals with arteries, veins, and nerve fibers. The Haversian system is several lamellae in the shape of an elongated bone length cylinder. The direction of collagen fibers in each adjusting lamella within this cylindrical ring or osteon are different, which creates the bearing strength (the space between collagen filled with bone salts). The bone is filled with lacuna cavities for osteocytes, connected with canaliculi, making the bone structure inhomogeneous. Perforating canals spread perpendicularly from central channels. All these interconnections serve as transport routes for nutrients. (Florencio-Silva et al., 2015)

A composition of spongy bone is aligned along the lines of stress applied to a bone. Trabeculae form the porous structure made of lamellae in an irregular arrangement filled with osteocytes connected with canaliculi. The composition of a spongy bone is surrounded by a compact bone (Doktor, T., Valach, J., Kytýř, D., Jiroušek, 2011). Organics contained in the bone are a source of carbon. Inorganic components of bone are composed of hydroxyapatite, which is a combination of calcium phosphate crystals and other mineral salts. The porous region of bone is an interconnected system (Krzesińska & Majewska, 2015).

The most abundant protein constituting extracellular matrix in mammals is collagen (see Figure 8). When pyrolysed, it produces eminently graphitized char owing to an aryl carbon vacancy promoting ring fusion. This condensation reaction results in the production of less volatiles and more stable char (Yamazaki et al., 2010).

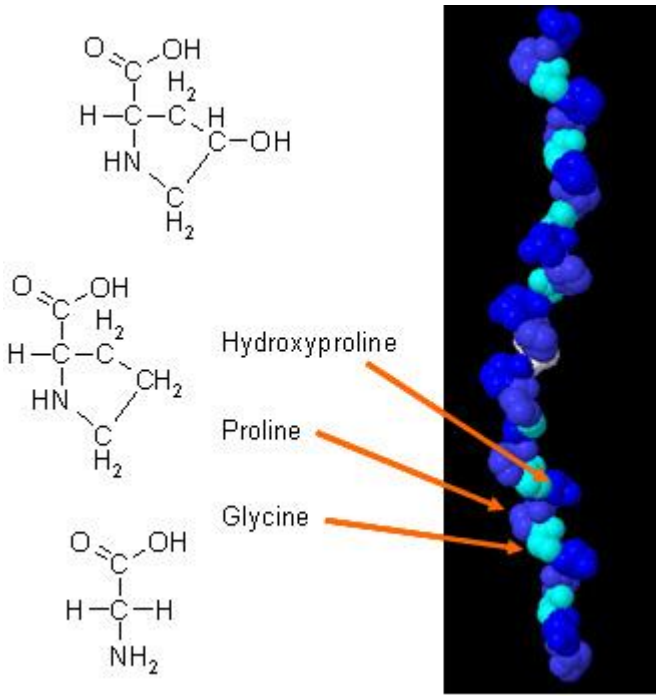

Figure 8 Collagen structure (Fanourgakis et al., 2020).

In bones collagen I is mineralised with hydroxyapatite. A bone is constituted of hydroxyapatite, which can be found around the collagen fibers. Some samples of bovine bone were pyrolysed to obtain a porous structure with a high surface area (Cazetta et al., 2014). During pyrolysis hydroxy apatite crystallises in the direction of a bone axis. The described structure was mostly composed of hydroxyapatite and had favourable for electroactivity pore size. Hydroxyapatites are able to promote electron transfer due to their perovskite structure. Thus, pyrolysed hydroxyapatites are used as catalysts (Proano-Aviles, 2020; Sambudi et al., 2016).

Blood contains cells (45%) and plasma (55%). Cells are the source of carbons. Also, plasma contains proteins and electrolytes. About 90% of plasma is composed of water. The electrolytes are represented by sodium (Na), chlorine (Cl), potassium (K), calcium (Ca), magnesium (Mg) ions. Nutrients are also present in the form of amino acids, minerals, and glucose. Urea is another product found in the blood. It is a nitrogen containing compound, like plasma in general.

Proteins are biopolymers that are scarcely present in both bones and blood. They might bring beneficial properties to pyrolytic products. Proteins consist of about 15% of nitrogen,

which is released in various forms during pyrolysis. The activation energy of proteins is relatively high (Guo et al., 2014).

2.2.2. Transitional metals

One way to reduce the cost of a catalyst is to replace the precious Pt with non-noble metals (Jaouen et al., 2011). The electrochemical activity of a catalyst can be compared to a commercially available catalyst after the incorporation of transitional metals within the carbon structure. The configuration and amount of the metals within a carbon structure define the electrical properties.

A catalyst can be functionalised with more than one compound (Strelko et al., 2000). Combinations of different metals include the interplay of the band gaps defining their conductive properties. The optimal donor-acceptor energetic characteristic for ORR and OER can be achieved with a transitional metal doping.

Transition metals (Yan et al., 2019; Yu et al., 2019) showed advantageous results for ORR (Noh et al., 2020) and OER (Xu Liu et al., 2018; Zou et al., 2019). The combination of transitional metals on a nanoscale will create more active sites for catalysis (Dou et al., 2016). This heterostructured nanointerface result in a high current density in bifunctional catalysts.

2.2.3. Developing a catalyst

Statistical and experimental methods can assist in the development of new materials. Computational techniques might assist in tasks where many variables are involved. The properties of precursor materials have an effect on the properties of the product, but the effect is not always direct. To predict the outcome of a production that has its own parameters various statistical techniques can be applied. However, machine learning can be used to automate the process aiming at the desired results.

Machine learning can be coupled with molecular simulations to predict the structure and behaviour of a material (Özkan et al., 2018, 2019). The accuracy of obtained results can be improved by providing more sets of data. The Praeto principle is usually applied in the

beginning stages of the analysis. In this way the algorithm is built on 80% of the data, and the rest is tested with statistical techniques.

Machine learning can be applied not only to improve the char for catalyst properties, but also to assist other procedures of the project. For example, further discussed development of a conductive ink formula can be optimized with machine learning techniques. There were many attempts to predict behaviour of a composition on the resulting electrochemical properties. The calculations were based on experimental work, that makes the procedure extremely time consuming. Application of machine learning is always straightforward, when dealing with quantitative data.

There are special techniques developed for energy storage devices, including catalysts (Özkan et al., 2018, 2019). Machine learning is widely developed in biomaterial related applications (*Holy Grail*, n.d.). Machine learning for battery development has already found its niche in the market. A company called Holy Grail (*Holy Grail*, n.d.) has set a benchmark to simplify the best performing battery production (Strelko et al., 2000).

3. Material and methods

This work is aimed at the development of the best performing catalyst derived from animal waste and transitional metals. The samples represented in Table 1 were prepared to investigate the influence of processing parameters and to compare the best performing materials.

The catalyst synthesis procedure was developed as a result of comparing methods and results of available publications. Many researchers explored animal waste pyrolysis to produce catalytic materials (Kumar et al., 2019; Xiaojun Liu et al., 2015, Guo et al., 2017; H. Wang et al., 2015). However, many methods involved strong alkalis that were meant to be excluded from the present research (Alonso-Lemus et al., 2019; C. Hu & Dai, 2017). Previous endeavours in this field informed the choice of best temperature regimes for the production of a catalyst from bone material (Dou et al., 2016; Huang et al., 2011; Krzesińska & Majewska, 2015).

In Figure 9 can be observed a code structure created to simplify the labelling of samples:

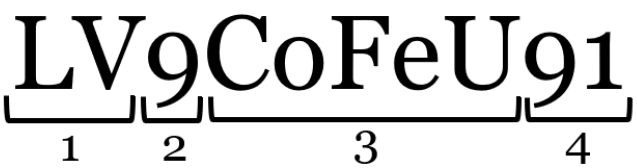

Figure 9 Sample name structure

1. precursor material(s) that can be L – bone (from the Finnish “Luu”). and V – blood (from the Finnish “Veri”);

2. temperature of the first carbonisation (i.e. the digit is to be multiplied by 100);

3. added materials, that may include cobalt (Co), iron (Fe), and urea (U);

4. each digit stands for a separate carbonisation temperature, with the second, being the temperature of the second carbonisation (i.e. 1 is to be multiplied by 1000).

Table 1 List of the samples analyzed in this work

Bone carbonized at 800 °C	Bone carbonized at 900 °C	Bone carbonized with heteroatoms	Bone and blood carbonized at 900 °C	Bone and blood carbonized with heteroatoms
L8	L9	LCo9	LV9Co9	LVCoFe9
L8Co9	L9Co9	LCo99	LV9Fe9	LVCoFe99
L8Fe9	L9Co98	LFe9	LV9CoFe9	LVCoFe91
L8CoFe9	L9Co99	LFe99	LV9CoFe99	LVCoFeU9
	L9Fe9	LCoFe9		LVCoFeU91
	L9Fe99	LCoFe98		
	L9CoFe9	LCoFe99		
	L9CoFe98	LCoFeU9		
	L9CoFe99	LCoFeU91		

The synthesised materials were compared to 20% Platinum on Vulcan XC-72R (FuelCell-Store) as a representative material for electrocatalysis.

3.1. Catalyst synthesis

Porous carbon was obtained by pyrolysis with the NBD Tube Furnace NBD-O1200-50IC. This work involves compressed gas, high temperatures, and corrosives safety precautions. The furnace has to be placed within a fume hood to prevent the escape of volatiles.

Bone meal (Solabiol) and bovine blood (Rönkä) were the precursor materials for the porous carbon preparation. Cobalt chloride (Sigma Aldrich) (Appendix A) and iron chloride (Sigma Aldrich) were used as a transitional metal source.

First, porous carbons were prepared by carbonisation of bone meal at 800 °C and 900 °C. Approximately 20 g of precursor material was placed evenly in a crucible and carbonised 2 h in an N_2 gas flow. Additionally, the mixture of bole and blood (1:1) was carbonised at 900 °C for 2 h. Heat rate was 5 °C/min in all cases.

To carbonise bone and blood with transitional methods, they were mixed with the metal chloride solutions were made. The metal precursor amount was chosen to be the same as the solid residue after bone carbonisation. This way 2,6 g of each metal precursor or their combination (1:1) were dissolved in 30 mL of deionized water. After the dissolution with the magnetic stirrer, the bone meal was added into the solution and stirred for 4 h to achieve the complete wetting of the bone.

Concerning the mixing of metals with blood, special consideration was taken to prevent blood coagulation upon contact with Fe. The blood (20 mL) was diluted with water (1:1). The 0.1 M solution of $FeCl_3$ was made out of 2.6 g or 1.3 g (if combined with Co) and added dropwise to the blood solution over continuous stirring, and this solution was then stirred for 2 h after the addition. Consequently, the solution was mixed in a 100 °C water bath for 2 h (Jian Zhang et al., 2015a).

The carbonised bone and bone with blood were mixed with metals in the same manner. 2.6 g of carbon were mixed with metal chloride solutions. Before carbonisation, all solutions were dried overnight at 60 °C. After carbonisation, each sample was leached by washing in 1 M HCl solution (see Figure 10).

Figure 10 Filtration setup.

The 300 mL of the HCl solution was mixed with the carbon on the magnetic stirrer overnight. The vacuum filtration assembly was used to wash away the acid. The 3 μm durapore hydrophilic membrane (Sigma Aldrich) was placed in a funnel connected to a filter flask. A vacuum pump was connected to the filter flask to speed the solution's flow through the filter. Deionized water was poured over the carbon in the filter until the filtered water would reach

a neutral pH. The washed carbon was collected and dried at 105 °C overnight. The weight of the carbon was recorded at this stage to estimate losses.

In both cases, the mixing of bone with metals prior to the carbonisation as well as the mixing of carbon with metals, the last carbonisation was followed by a secondary carbonisation occasionally. The secondary carbonisation was 1 h long and the temperatures were 900 °C or 1000 °C. The N_2 gas flow was maintained during the pyrolysis. The sample weights were recorded after each carbonisation. The carbon was not leached after the secondary carbonisation.

3.2. Physical characterisation

3.2.1. Surface area analysis

Micromeritics' TriStar II 3020 was used to measure the surface properties of the porous carbon samples. Attention has to be given to the use of compressed gases and low temperatures.

About 10 mg of a sample were placed in a sample cell, and the exact weight was recorded. The samples were outgassed to remove moisture and impurities in N_2 gas flow at 105 °C for 5 h. The weight of the samples after the degassing is recorded again. The amount of recorded points for a sample were from 0.06 g to 0.1 g and a waiting time of 10 s. The adsorption of N_2 is measured at -196.5 °C.

The BET and the Barrett-Joyner-Halend modes were used for an analysis of surface properties. The sample weight is recorded at the end of the experiment to determine the trustworthiness of the results. If the weight before and after the experiment is sufficiently different, the obtained data can be corrected in consideration the weight change per cent.

3.2.2. Raman spectroscopy

Renishaw 1000 UV was used for Raman spectroscopy. The laser exposure during the measurements must be prevented. The equipment used for the measurements contained 532 nm diode laser, an air-cooled CCD detector, and 2 gratings. The spectral collection

integration times for one acquisition were 20 s. The confocal aperture used of 50 mm was used during the measurements. It can analyze 1 mm square 2 mm deep area of the sample. The laser power was chosen to be 10 mW at the sample surface.

3.2.3. Electron microscopy

Zeiss Sigma VP was used for the scanning electron microscopy. The porous carbon was deposited on a double side carbon tape for SEM imaging. The air was blown on it to remove any loose particles. This will prevent them from detaching within the apparatus in a vacuum. Electron high tension was 10 kV with InLense. The viewing distance was about 5 mm.

Scanning transmission microscopy was performed with FEI Tecnai 12. The procedure requires safety precautions concerning low temperatures. A liquid nitrogen "trap" is used to prevent contamination of the microscope chamber. The 0.1 mg/mL ethanol solution was prepared with the porous carbon. The solution was deposited dropwise on a copper 3 mm grid. A strong magnet was used to remove loose particles from the grid.

3.3. Electroanalytical methods

Safety precautions concerning work with electricity and compressed gases must be taken into consideration for the following methods.

3.3.1. Conductive ink preparation

A catalyst was deposited on an electrode surface to estimate the electrochemical properties. Relating to this work, a glassy carbon electrode was used. A carbon-based conductive ink was prepared to withstand applied currents and interaction with an electrolyte.

In this study, the ink was prepared based on the polymeric anionic ionomer, which provides the binding of the carbon to the surface of the electrode, promotes wetting by an alkaline electrolyte, and conducts electrons sufficiently.

The inks were prepared to have 20 mg/mL concentration of carbon. A grade Ethanol was used as a solvent. Fumion® FAA-3 solution in N-Methylpyrrolidone (10%) was used as the

polyaromatic ionomer with quaternary ammonium functional groups. The exact formulation of FAA-3 is not available at the moment due to intellectual property rights on confidential information.

The ink was prepared as follows. 10 mg of porous carbon were mixed with 475 mL of ethanol and magnetically stirred for 1 h. 25 mL of FAA-3 was pipetted into the mixture of carbon and ethanol, and sonicated immediately for 10 min. After, the ink was left on a magnetic stirrer overnight. Right before the application, the ink was sonicated again for approximately 5 min.

3.3.2. Electrodes

3.3.2.1. Glassy carbon electrode

The glassy carbon electrode has a diameter of 5 mm and 0.196 cm^2 area. It is mounted into the rotation disc electrode with a length of 15 mm made of Teflon. Before the experiment, the glassy carbon electrode is cleaned on the polishing micro cloth nylon disks with a slurry of 0.05 μm alumina particles. Ethanol is used if any traces of the polishing slurry are left on the surface. The cleaning is finalized with sonicating the electrode for 1 min and drying for at least 20 min. Rotation disc electrode (Pine Research Instrumentation) has a length of 15 mm.

The conductive carbon ink is deposited on the glassy carbon electrode's surface prior to the electrochemical measurements. Due to hydrophobicity of the glassy carbon, the ink has to dry relatively quickly. If the drying is slow, the ink will aggregate around the edges, and the layer will not be homogeneous. A 2.5 uL drop of the conductive ink (concentration of carbon in ink is 20 mg/mL) was drop cast on the glassy carbon surface. This way 0.26 mg/cm^2 were deposited on the glassy carbon disc. A flow of air is immediately applied through a funnel for a uniform distribution. The ink on the glassy carbon electrode is placed under the flow and slowly rotated to even dry. The electrode must not be tilted during the drying. The airflow is gradually increased as the ink dries. After the ink is dried, which can be confirmed by visual examination, the electrode is placed in an oven at 70 °C for 20 min for the ionomer to solidify. This will prevent the loss of the catalyst during the experiments.

The precision of measurements is highly dependent on the quality of the carbon layer on the electrode. The carbon layer was removed by polishing the electrode with an aluminum paste (Pine Research Instrumentation). Furthermore, the formation of the oxygen bubbles within the carbon pores requires new carbon layer after each OER sweep.

3.3.2.2. Electrochemical cell

The electrochemical measurements with the glassy carbon electrode were performed in a three-electrode cell set up connected to the Wavedriver 200 EIS Bipotentiostat/Galvanostat (Pine Research Instrumentation). The reference electrode was Ag/AgCl. It is noted that the Ag/AgCl is not stable in alkaline solution. The counter electrode was a platinum wire. The configuration of three electrodes in an electrolyte solution can be observed in Figure 11. The dual-port gas inlet allows both purging and sparging of the air from the cell, replacing it with inert gas, argon (Ar) in this case.

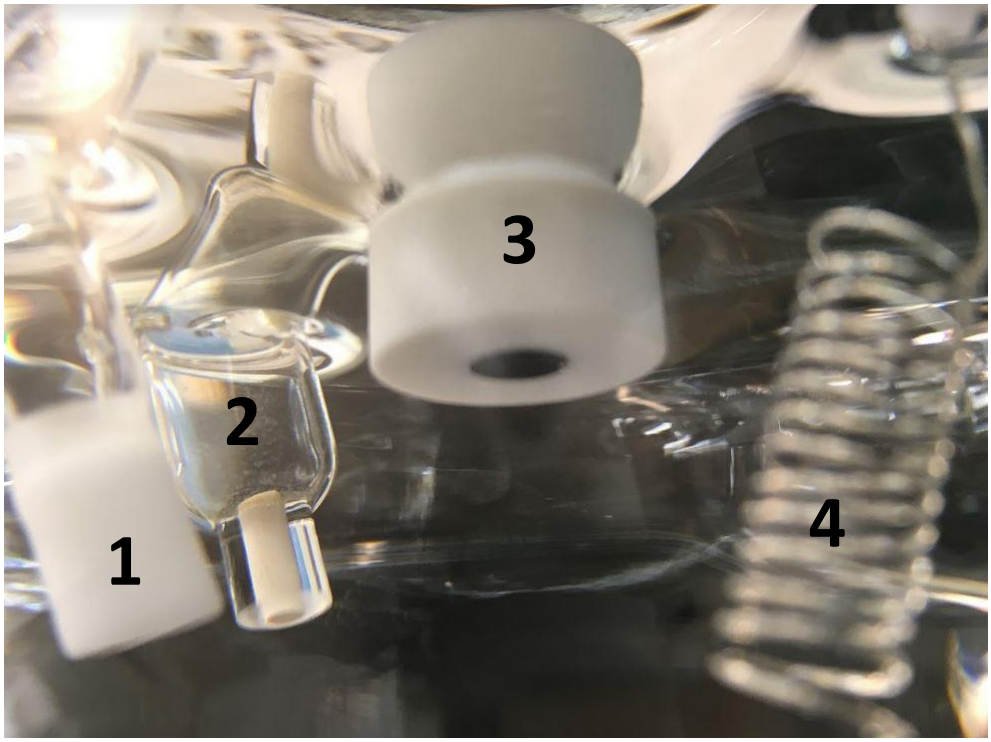

Figure 11 Inside the electrochemical cell containing electrolyte (from left to right): 1) gas inlet; 2) reference electrode; 3) working electrode; 4) the counter electrode;

The electrochemical cell represents a glass 150 mL flask with five round ports compatible with the electrodes and the gas inlet. It was filled with 0.1 M potassium hydroxide (KOH) electrolyte solution. Standard atmosphere pressure conditions were maintained during all experiments.

3.3.2.3. Gas diffusion electrode

The reactant gases enter the gas diffusion electrode (GDE). The GDE is a porous material that ensures the reactants from gas and electrolyte access the catalyst layer. The GDE is waterproof to ensure that its pores do not become obstructed with liquids. In this way, the GDE assist in water management by allowing an appropriate amount of water to reach and be held at the membrane. Gas and water vapor from the anode catalyst layer travels through the electrolyte and is then adsorbed at the electrode surface. Adsorbed species might migrate along the solid electrode surface mainly by diffusion. The reaction gives rise to protons and electrons.

GDE represents the catalyst deposited on a supportive diffusion Teflon substrate (Biplex gaskatel) (see Figure 12). This configuration brings the solid catalyst, gas, and the electrolyte into contact with each other. The substrate is attached to the nickel mesh. The suitable for the cell diffusion support was cut out with a 15 mm gasket punch. The aforementioned electrochemical ink was drop cast on the support to deposit 2 mg/cm^2 of the carbon catalyst. The electrode was dried at 70 °C for 15 min.

Figure 12 Gas diffusion electrode setup: 1) GDE; 2) gas tube; 3) current collector; 4) electrochemical cell.

The electrode was placed within a Teflon tube with a fastening cup for the electrode at one end. The nickel mesh on the electrode is pressed against a platinum wire mesh current collector, which goes across the Teflon tube. The other end of the tube has an inlet and an outlet for gas to circulate around the electrode.

The setup for the gas diffusion electrode measurements resembles the cell for the glassy carbon electrode (see Figure 13). The open-top glass cell (Adams & Chittenden Scientific Glass) has one inlet on the side for the Teflon tube with the working electrode. The tube is fastened with a knuckled clamp to seal the cell opening. After the electrolyte is placed in the cell, a lid with round inlets for counter and reference electrodes is placed on top of the cell. The counter and reference electrodes used were described previously. Finally, the working electrode is connected to the gas inlet and a platinum wire current collector enclosed in a Teflon tube attached to the cell's side. In this configuration, the magnetic stirring provides the mixing of the electrolyte, which supports the transportation of ions to the working electrode. The protocol for GDE measurements can be found in Appendix E.

Figure 13 Gas diffusion electrode setup connected to the potentiostat: 1) counter electrode; 2) reference electrode; 3) working electrode.

3.3.2.4. Electrochemical characterisations

When a potentiostat produces a chosen potential, the actual potential that is exerted differs slightly from the specified value. This happens due to resistance in the hardware. To account for the losses and adjust the signal to the real potential, the iR correction has to be performed at any time electrochemical measurements are performed.

The impedance spectroscopy measurements are used to estimate the difference between the programmed and the real potentials. The working electrode connected to the WaveVortex® 10 (Pine Research Instrumentation) was rotated during OER and ORR measurements (see Figure 14).

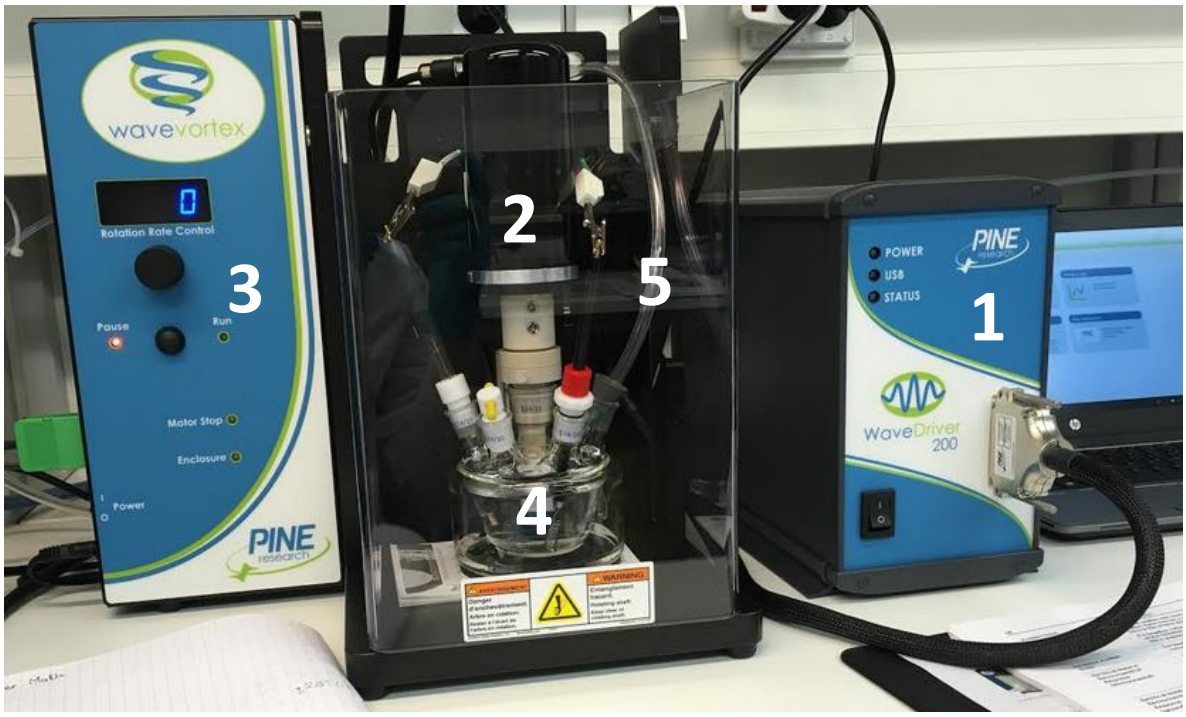

Figure 14 Three-electrode cell connected to rotor and potentiostat: 1) potentiostat; 2) rotor; 3) rotor control; 4) electrochemical cell; 5) gas tube.

Appendix D contains a protocol for the glassy carbon electrode measurements. It was developed to facilitate the activation and preservation of the carbon layer simultaneously. The chosen method was designed to maximise the precision of the obtained data. A sequence of methods can be created in the Aftermath software to facilitate the data collection's automatic flow. When protocol requires, a sequence must end to allow the manual change of a purging gas. Chronoamperometric measurements also have to be performed separately from a sequence. This allows an operator to ensure that the electrode is in functional condition and the gas flow is adequate prior to the timeous measurement.

Before the experiment, the electrolyte solution in the cell was purged with Ar gas for 30 min. During the experiment, the gas was sparged above the surface of the electrolyte solution to prevent ambient gas access.

Two equal electrodes were prepared with each analyte. The RDE electrodes were tested according to the protocol in Appendix D. Each electrode was subjected to cyclic voltammetry (CV) first to provide sufficient wetting of the catalyst porous surface. With each cycle, the rate of the reaction grows. At the same time, the potential window for the electrochemical measurements can be determined at this stage. The range is characteristic to each material; that is why the newly developed porous carbon catalyst activity has to be explored in the

beginning. The first cycle of the CV was performed in a window that was previously reported for similar material. Consequently, it was adjusted to represent the oxidation/reduction reactions fully.

After that, the electrode's resistance was estimated by electrochemical impedance spectroscopy – uncompensated resistance (EIS-RU). The following CV is conducted to evaluate the reduction/oxidation behaviour of the catalyst more precisely. This time, the Aftermath Software provided iR correction automatically, which was calculated after the EIS-RU.

Until now, the method did not employ the rotation of the working electrode. The rotation rate per minute can be programmed in the Aftermath software for the ORR and OER measurements. The chronoamperometry stability method requires manual rotation speed set up.

3.3.2.5. Voltammetry

For current to flow, voltammetry requires a three-electrode cell setup to vary potential at a working electrode. This can be achieved by introducing a counter electrode that will induce the current from the working electrode. While a reference electrode is connected to a voltammeter, the counter and the working electrodes are connected to a power source.

A working electrode is embedded in a polymer cylinder and shaped like a disk on its surface. The electrode is usually made of platinum, gold, or carbon that provides inertness during electrochemical reactions within a given condition. The durability of the electrode is an intrinsic quality as it affects the performance and accuracy of measurements. The working electrode must provide the absence of background current in the absence of reactive species.

Potentiometry non-standard potential of a cell can be related to the concentration of reduced and oxidised ions, the concentration of an analyte can be measured. The setup for measuring potential is as follows—voltmeter connected to electrodes. One is a working electrode and a reference electrode. Electrodes are submerged in analyte solution in an electrochemical cell.

The voltage difference is maintained between reference and working electrodes, and the current flows in an oxygen purged electrolyte solution between the counter and working electrode. Potential is measured with respect to the reference electrode. Electrolyte solution carries the charge and decreases the mobility of ions due to electrostatic attraction. The ions migrate in the solution towards a charged electrode, creating a current as being attracted

electrostatically. The migration can generate current by diffusion through a concentration gradient or convection when the electrolyte is stirred.

The working potential is measured between the analyte solution and the working electrode. Furthermore, the reference potential is measured on the reference electrode. The cell potential is equal to the difference between working and reference potentials.

In the absence of the net current flow, the open-circuit voltage can be measured when the potential difference is applied. In the first case of current flowing through the cell, the cathodic potential is lower, and the anodic is higher. Thus, cell voltage at the closed circuit is smaller than the open-circuit voltage. The difference between open-cell and cell cathodic potential is the overpotential.

The reference electrode potential is usually expressed in terms of hydrogen electrode. Hydrogen electrodes are complicated to use due to hydrogen reactivity and complications in maintaining the gas concentration. There are different reference electrodes available, varying in the reference material. Results obtained with any electrode can be converted to correspond to hydrogen electrode measurements.

3.3.2.6. Oxidation and reduction

CV is an electrochemical experiment that is based on a gradual increase and decrease of potential overtime in a cyclic manner. Nernst Equation 11 can describe the oxidation and reduction behaviours of a working electrode dependent on the electrochemical reactions' reduction potential (Fourmond & Léger, 2019). In this way, the concentration of oxidised and reduced molecules varies with the applied potential at a particular moment. The cycling of the potential allows control over oxidising and reducing processes. The measurements are dependent on the temperature and the electrolyte.

$$E = E_0 - \frac{RT}{zF} \ln \frac{[Red]}{[Ox]} \quad (11)$$

During the process ions from an electrolyte are adsorbed at the electrode surface, forming a double layer. The diffusion rate and availability of the ions through the double layer

towards the electrode define the current. In other words, a current is produced when the ions undergo the oxidation or reduction reaction. The change in current occurs when the ratio between oxidised and reduced species is changing.

When potential is swept positively, the ions are oxidised, which produces anodic current. The average of peak anodic and cathodic potentials is the current, which, when oxidised species and reduced species concentrations are equal, corresponds to half potential ($E_{1/2}$).

The standard potential of a redox reaction (E_o) in the Nernst equation is located between cathodic peak (E_{pc}) and anodic peak (E_{pa}) potentials. The E_o is smaller than E_{pa} and larger than E_{pc}. The E_o should be higher than E_{pc}, when the amount of reduced species is increased.

Stirring is never applied in the cyclic voltammetry as it restricts the formation of the double layer. The Nernst equation requires a double-layer diffusion coefficient of available charged species.

3.3.2.7. Electron transfer

The number of transferred electrons must be determined before the oxidation/reduction measurements. As described before, the ORR and OER are four-electron transfer reactions. If the calculations result in a bigger or smaller number than four, troubleshooting is performed to ascertain why.

Increasing a scan rate increases the peak current in reversible processes, as more electrons flow. An irreversible process is characterised by a slow electron transfer relative to the scan rate. In this case, the peak voltage shifts. As the potential swept towards negative voltage, the oxidant species have more positive reduction potential. The electrons can transfer when the energy of the electrolyte's lowest unoccupied molecular orbital is lower than of the vacant highest occupied of the. This is a reduction. (Strelko et al., 2000)

Kinetic control is used to vary the charge transfer rate at an electrode with the reaction speed. To establish behaviour of the reactions, the electrode is rotated at different rates resulting in the range of current densities as the applied potential grows (see Figure 15). This difference is due to a change in mass transfer. In a mass transfer control, the speed of a reaction is limited by a diffusion rate. In the absence of kinetic control, the charge transfer and diffusion are equal.

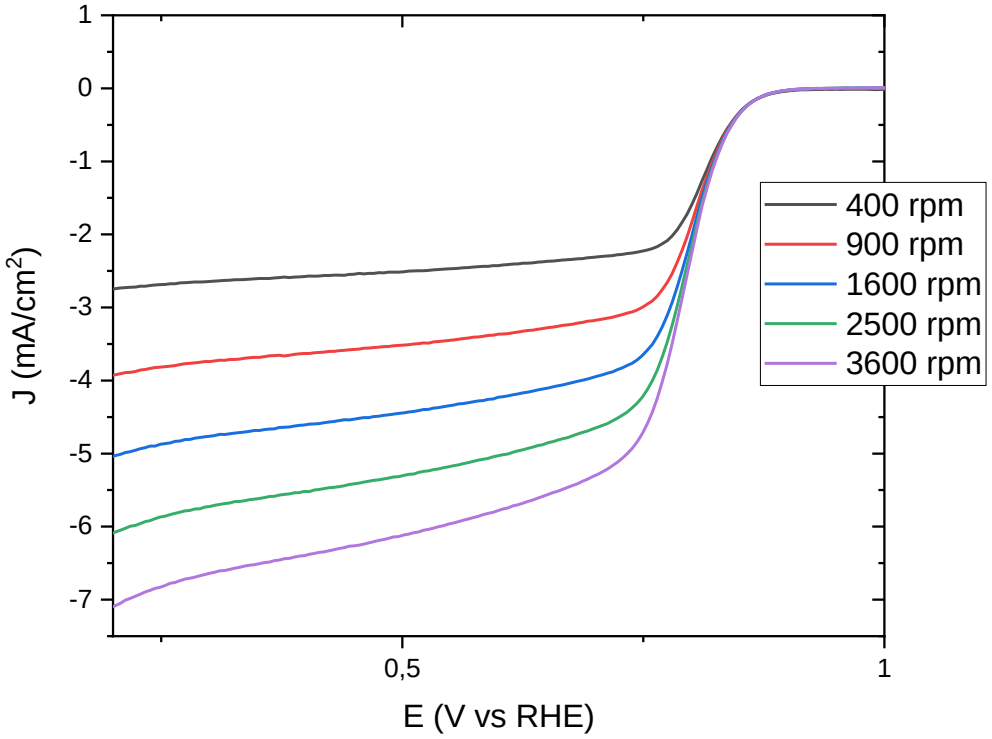

Figure 15 ORR at different electrode rotation speed.

An electrode supplies electrons, which reduce protons in a solution, producing water or peroxide. The concentration of a reactant in a solution stays high, while it is significantly lower on an electrode's surface.

$$i_{LC} = 0.62 \times n \times F \times A \times D_0^{2/3} \times v^{-1/6} \times \omega^{1/2} \times C_0 \qquad (12)$$

To determine the mass transport and diffusion around RDE the Levich equation (see Equation 12) is used (see Figure 16, 17). The equation uses the number of electrons transferred, the diffusivity of the oxygen as a reactant, the kinematic viscosity of a solution, the electrode's angular velocity, and the oxygen concentration in the solution.

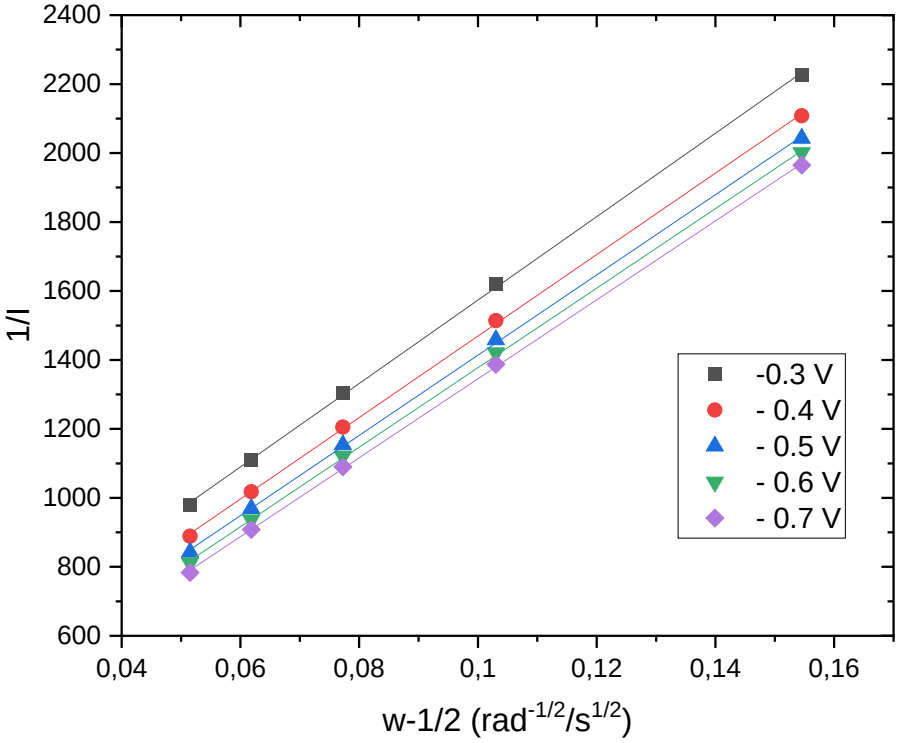

Figure 16 Koutecky-Levich plot.

$$I_L = (0.62) \times n \times F \times D_0^{2/3} \times v^{-1/6} \times \omega^{-1/2} \times C_0 \quad (13)$$

Where I_L - Levich current (A) (see Equation 13), n - the number of electrons transferred in a half reaction , F - Faraday constant (C/mol), D_0 - the diffusion coefficient (cm²/s), ω - the electrode angular rotation rate (rad/s), v - the kinematic viscosity (cm²/s), C_0 - concentration of the analyte (mol/cm³), A – area of an electrode (cm²).

$$\frac{1}{I_L} = \frac{1}{I_K} + \left(\frac{1}{0.62 \times n \times F \times A \times D_0^{2/3} \times v^{-1/6} \times C_0}\right)\omega^{-1/2} \quad (14)$$

The Koutecky-Levich equation (see Equation 14) inverse of the total current on a disc electrode can be expressed as a sum of its kinetically controlled current and the inverse of the mass transport control current (Bard et al., 2001).

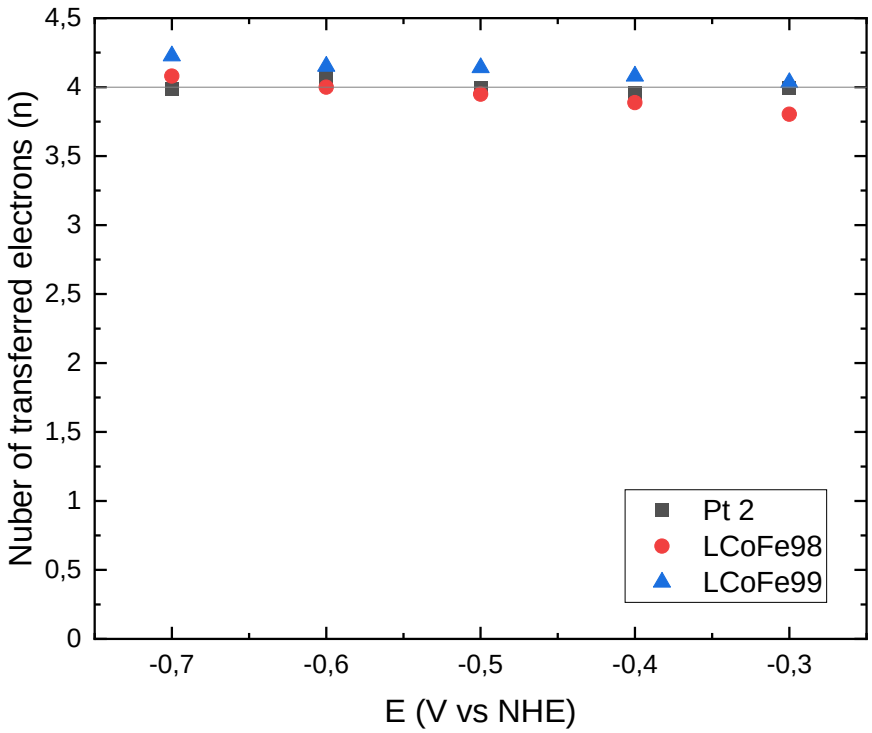

Figure 17 Number of electrons transferred for the ORR obtained from K-L plots.

3.3.2.8. Collection efficiency

The products, which are formed on an electrode surface when multiple chemical pathways are possible, must be identified and quantified. A ring electrode surrounds a disk electrode with an insulating material in between them. The insulating material is often Teflon.

$$H_2O_2\% = \frac{n-4}{2} \times 100 \qquad (15)$$

An oxygen reduction with two or four electron-pathways will occur on the disc electrode. The reaction products, namely water and peroxide, are transported to the ring electrode by the flow. Only selective reoxidation is allowed on the ring electrode as it is poised at a specific potential. In this way, only hydrogen peroxide will be reoxidised on the ring electrode (see Equation 15). The potential on the ring electrode can be E=1.2 V vs NHE.

The total disk current is formed by current due to peroxide formation and current due to water formation.

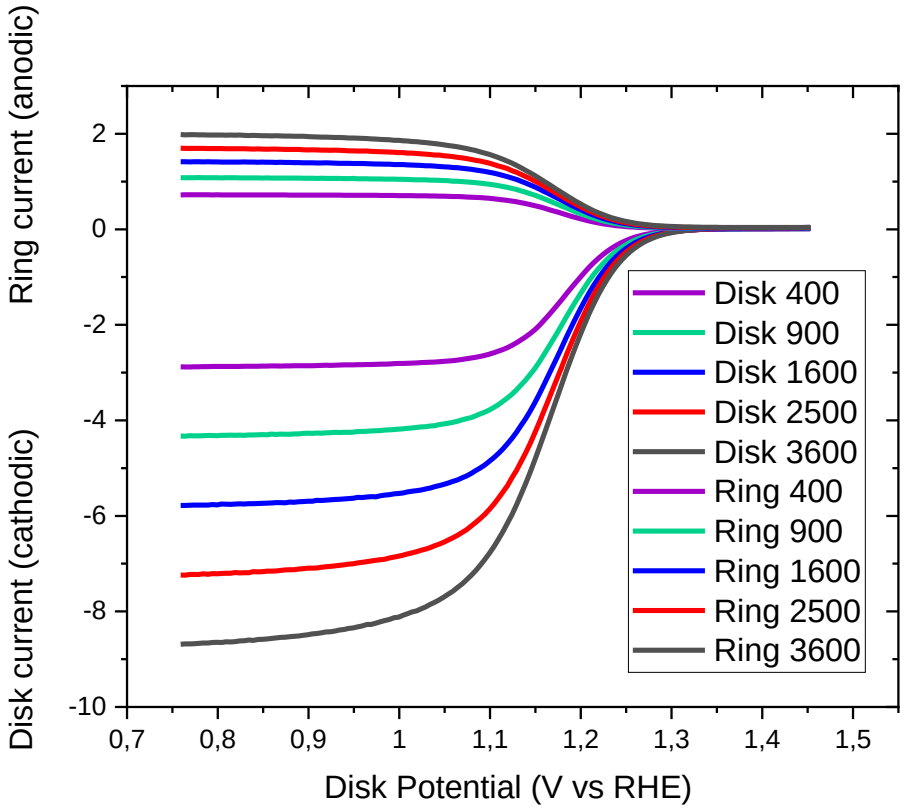

Figure 18 Rotation ring disk electrode voltammograms at various rotation rates.

$$n = \frac{4 \times I_d}{I_d + \frac{I_r}{N}} \tag{16}$$

The electrode's collection efficiency is expressed as a relation between a current at the ring electrode and a current at the disk electrode (see Equation 16). It signifies a fraction of the species produced on the disk, which are transported to the ring and react with it. The collection efficiency is a function of the geometry of both electrodes. It is determined empirically prior to experiments. Rotation is required to create a laminar flow at a surface of the electrode (see Figure 18).

3.3.2.9. Stability

Constant voltage is applied, and current is monitored to test a catalyst stability during chronoamperometry. This method can determine how long a catalyst can be subjected to the constantly applied potentials. The work of the electrode material is simulated, and a long-lasting experiment will define a catalyst's stability over time.

Stability of a catalyst can be studied by performing the CV method measuring the decrease in the voltammetry peak current during potential cycling, or by comparing its initial response with its response after storage in standard conditions over several days.

The Cottrell equation describes materials, whose current density decreases over applied potential. The behaviour of a catalyst during chronoamperometry in terms of Cottrell equation records the electric current with respect to time. At some point of the measurements the produced current will stabilise as only diffusion produces reaction. The stability chronoamperometric measurements are sensitive and depend on multiple parameters and conditions, as described above (Kamat et al., 2010).

3.4. Trustworthiness of the study

To ensure the trustworthiness of the study, a quantitative analysis was performed to establish the repeatability of the results. Not merely human error, but also a modification in equipment or ambient conditions might affect the results. If the results variate too much, they cannot be accepted. Variation between values can be accessed by estimating standard deviation. Table 2 shows the correlation between results, that are no more than 5%, which is a permissible value.

Table 2 Variation coefficients of weight loss and BET surface.

	Initial weight, g	Weight after pyrolysis, g	Weight loss, %	BET, m^2/g
L8	22.10	12.37	44.02	692.83
	25.12	14.03	44.15	675.29
	22.17	13.12	40.83	658.32
		avg	43.00	675.48
		st	1.88	17.25
		rsd, %	4.38	2.55
L9	24.46	12.99	46.90	692.29
	36.10	19.74	45.33	691.81
	25.09	13.89	44.65	747.83
		avg	45.62	710.64
		st	1.15	32.21
		rsd, %	2.53	4.53
LV9	40.00	11.56	71.09	517.81
	38.56	10.35	73.16	516.48
	40.00	11.09	72.28	531.01
		avg	72.17	521.77
		st	1.04	8.04
		rsd, %	1.44	1.54

The precision of a signal is dependent on an electrochemical ink's quality. Also, electrochemical measurements are extremely sensitive to all parameters. The preparation method and electrochemical testing results were analyzed to ensure repeatability. Figure 19 shows that the number of electrons transferred is the same for the same materials prepared on different days.

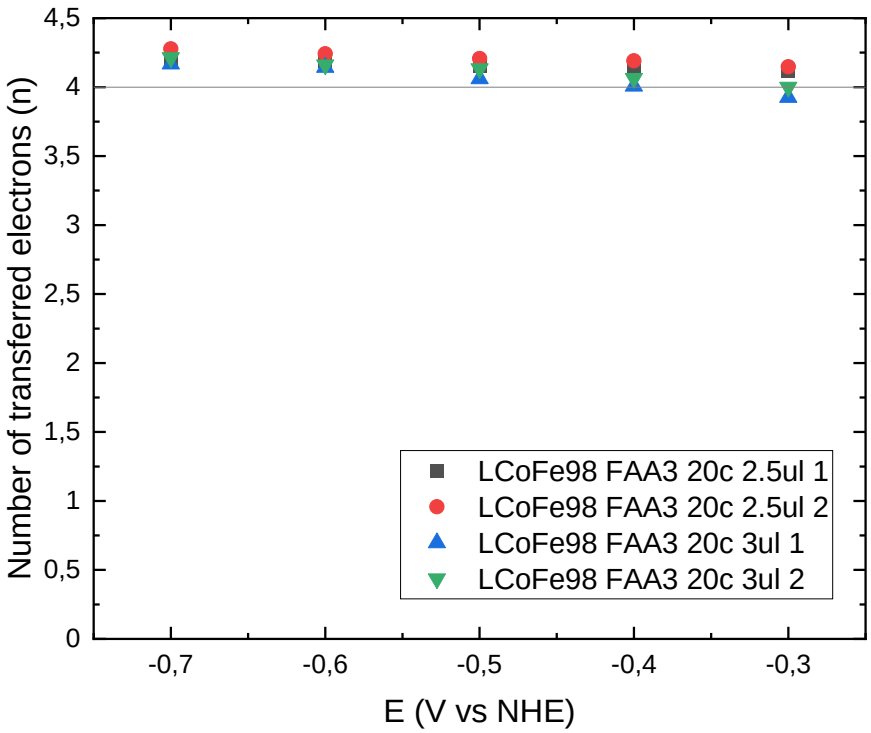

Figure 19 Number of electrons transferred in different samples of the same composition.

4. Results and discussion

The practical work focused on the development of a catalyst for ORR and OER. To account for various parameters, 26 samples of porous carbon were produced (see Table 1). Further, the influence of mixing methods, composition, and pyrolysis conditions were discussed. With regards to its electrocatalytically properties, one sample stood out more than others. It was produced by carbonising the mixture of bone and Co and Fe. During the analysis, an emphasis was given to the sample LCoFe99, as mentioned above. The results of the porous carbon synthesis and analysis are presented below.

Physical characterisation is crucial for an interpretation of electrochemical results. Understanding the interconnection of structure with electron transfer behaviour may assist in future improvement of specific characteristics. Some results are also attached in Appendices.

The structure of the results and discussion section is divided according to the following categories:

1. The effect of pyrolysis temperature;
2. The effect of mixing sequences;
3. The effect of precursor composition.

4.1. Physicochemical characterisations

An analysis of the structure of the doped porous carbon catalyst is summarised in Figure 20. The samples that are compared on the graphs are bone carbonised at 800 °C and 900 °C. And these two carbons pyrolysed at 900 °C with addition of transitional metals.

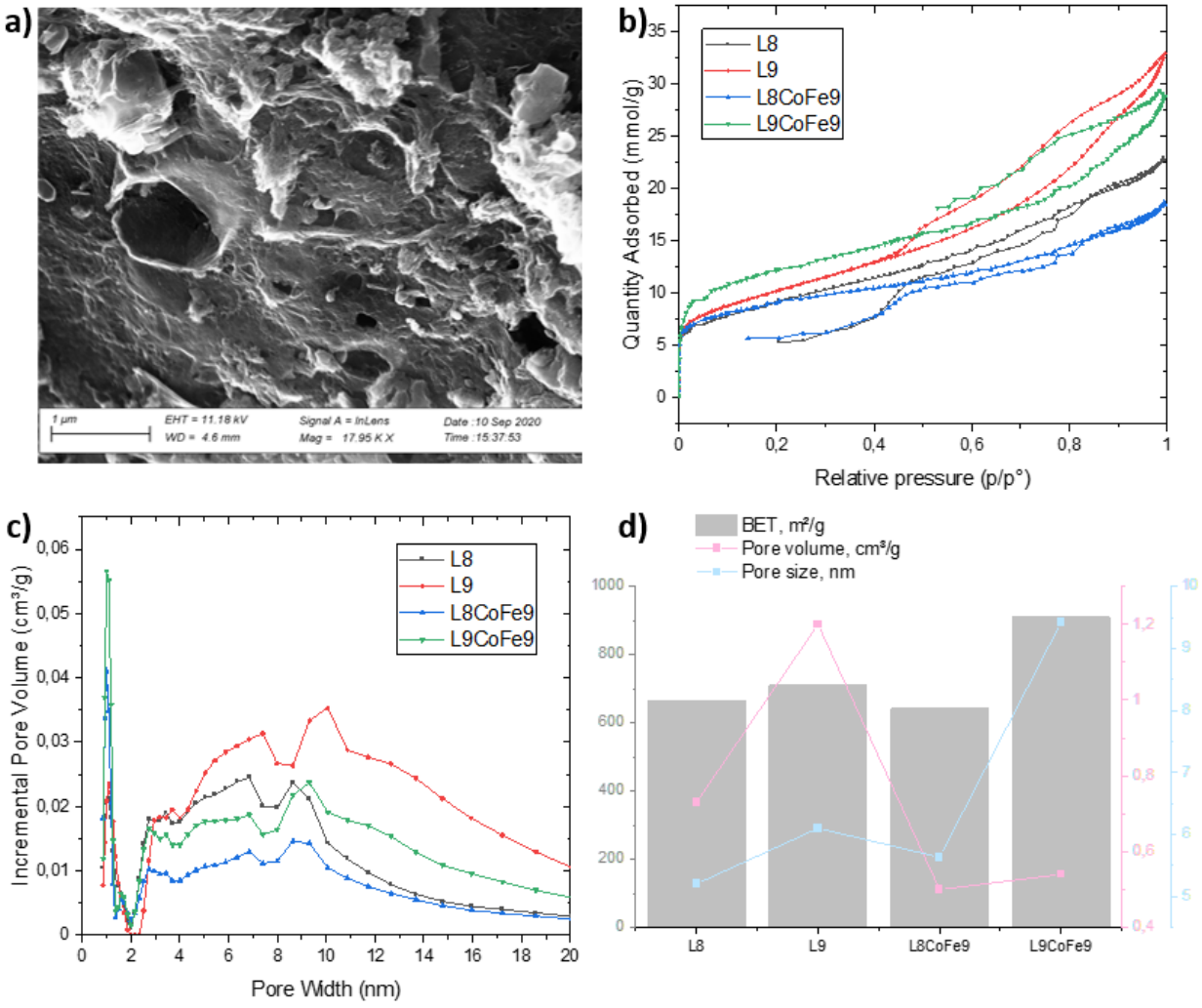

Figure 20 a) Surface morphology, SEM image; b) Adsorption isotherms; c) Pore size distribution; d) BET surface and pore properties.

The porous structure consists of pores, which on average range in size between 5 and 9 nm (see Table 3). The pores are formed by a morphology of the precursor bone that consists of collagen fibers and minerals. Moreover, the products of pyrolysis like volatiles and tar promote the nanopore formation on their escape. Finally, the acid wash after pyrolysis washes out residues and forms the pores in the structure.

The SEM image represents the microstructure of the carbons (see Appendix C). The nanostructure can be analyzed by N_2 adsorption isotherms and the pore density distribution. Adsorption isotherm for all samples has a hysteresis loop. It is located at the relative pressure >0.4 that corresponds to a mesoporous structure. TEM images could become a source of information concerning the interior of the porous carbons. However, due to magnetism

of the catalyst the electron beam was diffracted, resulting in blurred images (see Appendix B).

Pore volume distribution shows a sharp peak around 1 nm, especially for bone carbonised at 900 °C and mixed with metals. The specific BET area is also the largest for this sample. In fact, all the samples have a relatively large BET surface for carbons prepared in the similar manner (H. Song et al., 2014; R. Wang et al., 2015). At the same time the pore volume distribution pattern is similar to that in porous carbons derived from animal bone (Huang et al., 2011; Patel et al., 2015).

Table 3 Effect of pyrolysis temperature on surface properties.

	BET, m^2/g	Pore volume, cm^3/g	Pore size, nm	Micropore volume, cm^3/g	Total volume, cm^3/g	Micropores %
L8	665.48	0.73	5.20	0.13	0.58	22.68
L9	710.64	1.20	6.10	0.13	0.77	16.51
L8CoFe9	641.32	0.50	5.63	0.18	0.47	39.39
L9CoFe9	909.35	0.54	9.42	0.24	0.73	32.47

By analyzing data in Table 3 it can be seen that the temperature of carbonisation affects surface morphology and pore qualities. A higher temperature of carbonisation results in a larger BET surface area, pore volume and size. This can be attributed to a more rapid escape of pore forming volatiles during pyrolysis.

The addition of metals to the carbonised bone at 900 °C result in an increase in the BET area. However, the micropore volume and percent increases. This might be caused by attachment of the metals that divide already existing pores to smaller ones. This does not happen when the bone carbonised at 800 °C is mixed with metals. It can be explained as L8 has smaller pores than L9 and this might prevent the access of the metals within the carbon structure for attachment.

Carbon produced from bone mixed directly with metals prior to pyrolysis has a slightly different surface morphology (see Figure 21). The main distinct feature that can be noticed from the SEM image is the presence of anchored functional groups. Due to the fact bone has a much larger pore size than carbonised bone, it is much easier for metals to protrude inside the bone structure.

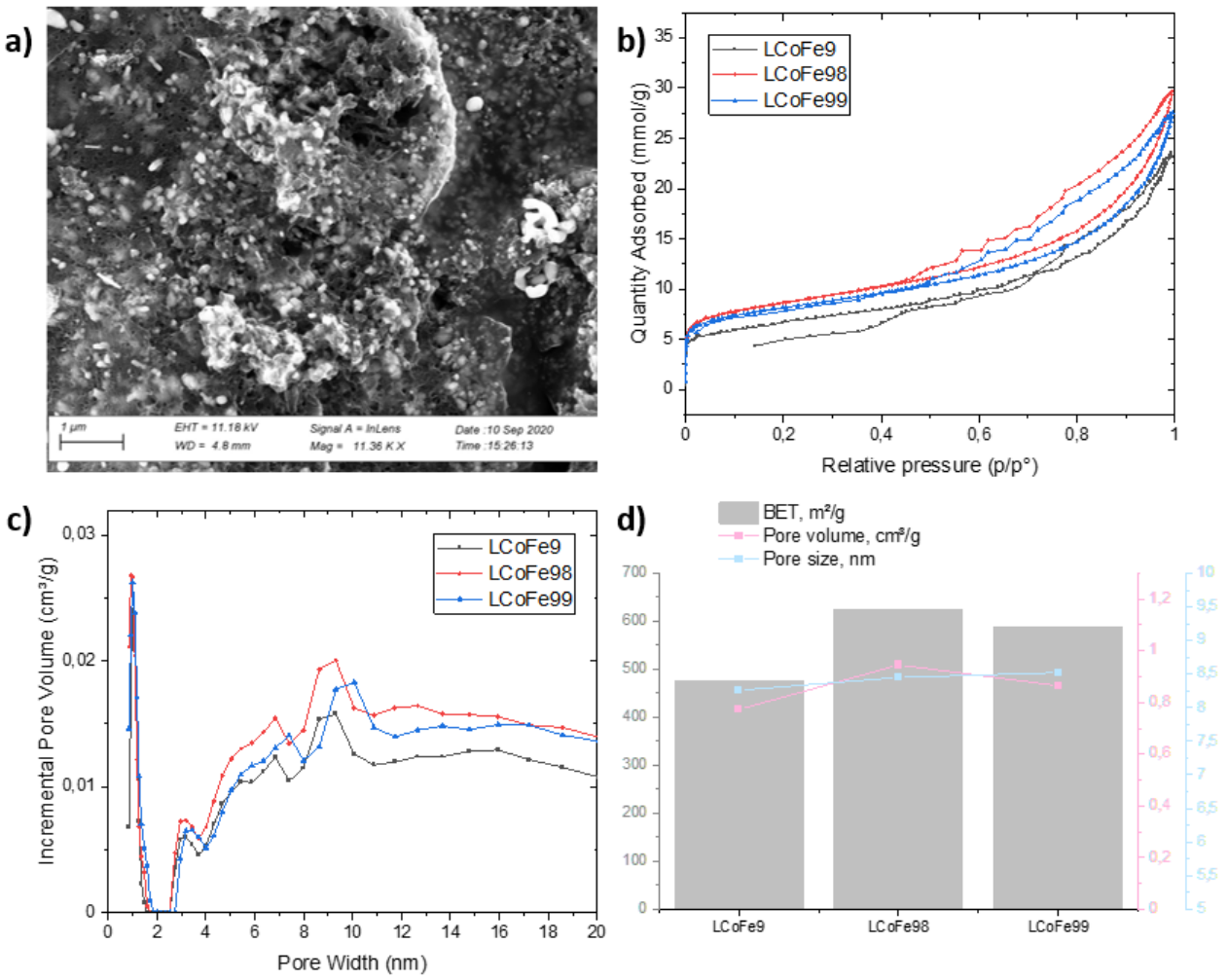

Figure 21 a) Surface morphology, SEM image; b) Adsorption isotherm; c) Pore size distribution; d) BET surface and pore properties.

Pore volume distribution shows a peak around 1 nm for the bone carbonised alone. However, the incremental pore volume for latter samples is twice smaller. The pattern of adsorption isomers is similar, and also indicate mesoporous pore structure.

The BET surface is significantly reduced. The metals might have blocked many pores. Micropore percent is also low. The porosity of bone carbonised with metals is worse than carbon pyrolysed with metals (see Table 4).

Table 4 Dependence of surface properties on second carbonization.

	BET, m^2/g	Pore volume, cm^3/g	Pore size, nm	Micropore volume, cm^3/g	Total volume, cm^3/g	Micropores %
LCoFe9	476.68	0.77	8.26	0.10	0.48	20.42
LCoFe98	625.21	0.95	8.45	0.14	0.64	22.68
LCoFe99	588.06	0.86	8.52	0.14	0.59	23.78

The effect of the secondary carbonisation on the morphology of the carbon samples can also be analyzed (see Table 5). BET surface does not show a direct dependence on the temperature of the secondary carbonisation. Neither does, the pore volume follow a change in the secondary pyrolysis temperature. The pore size is slightly increasing. Secondary pyrolysis is performed to stabilise the structure of the carbon. During the secondary pyrolysis minimal structural changes take place. Accordingly, the pore properties do not vary significantly.

Table 5 Effect of the secondary carbonisation on the morphology of the carbon.

	BET, m^2/g	Pore volume, cm^3/g	Pore size, nm	Micropore volume, cm^3/g	Total volume, cm^3/g	Micropores %
L9CoFe99	949.20	0.86	5.87	0.26	0.77	33.24
LCoFe99	588.06	0.86	8.52	0.14	0.59	23.78

Consequently, many differences can be noted, if samples with a different order of mixing, but of the same carbonisation regime and composition are compared. By further analyzing electrochemical properties it would be possible to see the influence of the surface morphology.

Raman spectroscopy allows determination of a carbon structure. In Figure 22, two peaks that are seen represent sp2 orbital vibrations (first D peak) and sp3 orbital movements (second G peak). The ratio between integrated areas of these peaks represents the disorder of the graphene structure. Catalyst obtained by pyrolysis of mixture of bone and metals result in D/G equal to 0.93. The same sample, which underwent 800 °C secondary pyrolysis, has D/G of 1.02; and at 900 °C secondary pyrolysis resulted in D/G of 0.86.

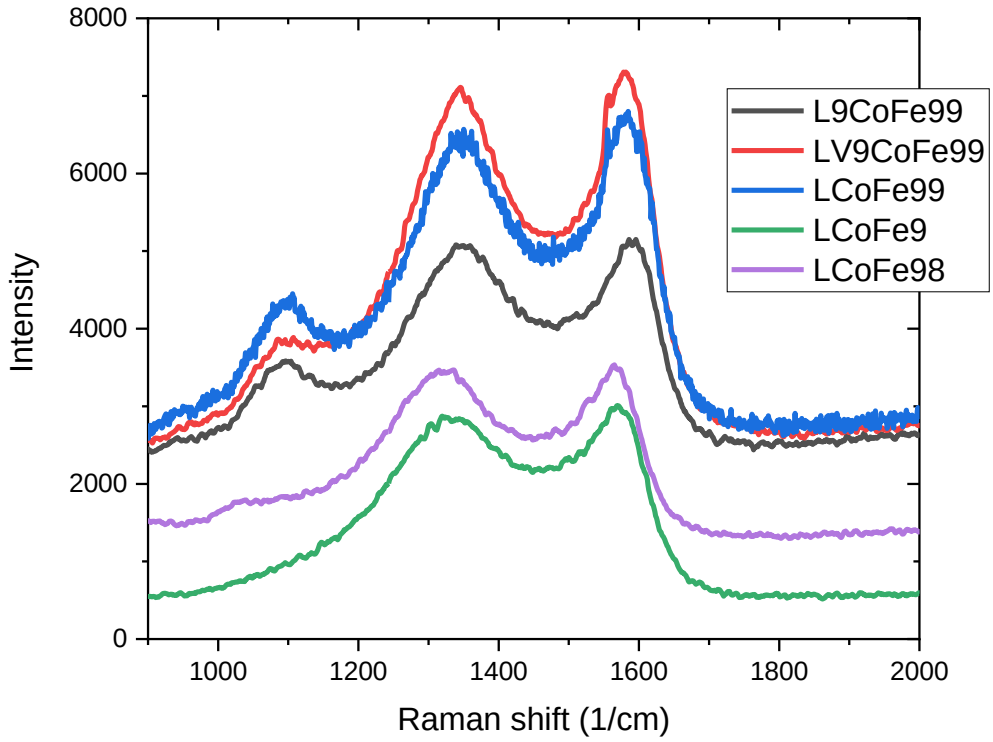

Figure 22 Raman spectra of carbon region for samples with different composition and secondary pyrolysis temperature.

4.2. Electrochemical characterisation

To analyze the catalytic activity of the functionalised porous carbon the CV measurements were performed first. The example in Figure 23 the difference in CV in O_2 and N_2 can be seen. For our samples, the ORR peak was revealed near 0,8 V (RHE) for our samples. Also, the presence of the anodic peak at 1,02 V signifies a reaction that involves Co. Interestingly, the CV shows two small anodic peaks at the 1 V potential. The origins of the reactions are unknown and do not appear in other literature (M. Zhang et al., 2017).

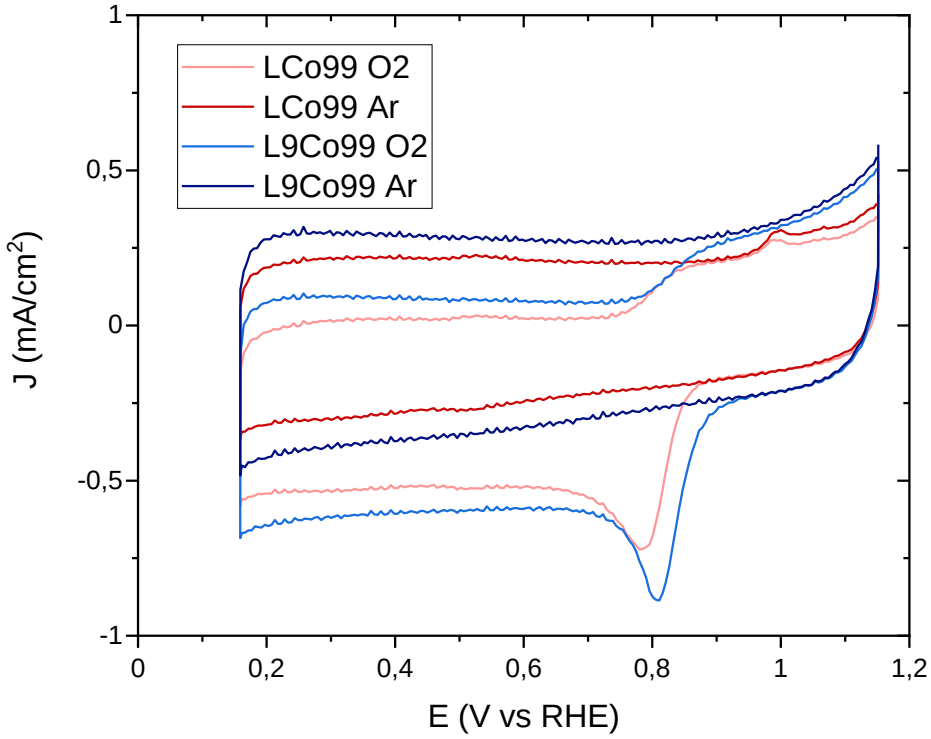

Figure 23 CV of catalysts containing Fe, Co in 0.1 M KOH electrolyte saturated with Ar and O_2.

From the example in Figure 24 the difference in the catalytic activity can be seen for samples with the same composition and carbonisation methods. LCoFe99 shows a smaller double layer capacitance due to lower BET surface area than the other two samples. However, the ORR peak potential is larger for LCoFe99 (0.81 V) than for L9CoFe99 (0.8 V).

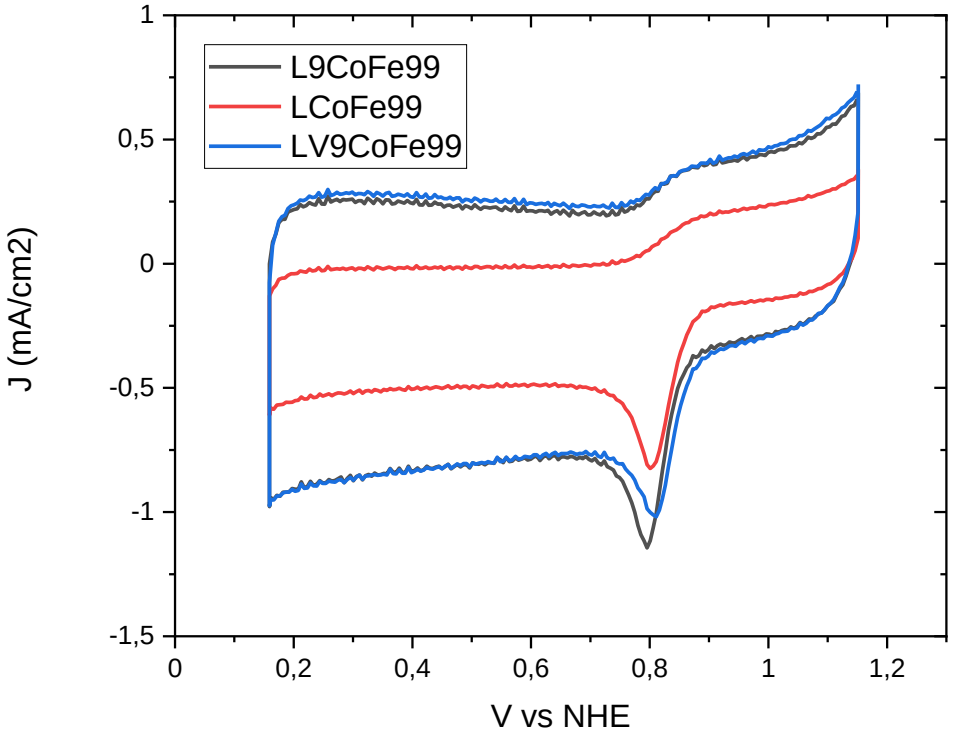

Figure 24 CV of samples with different composition in 0.1 M KOH electrolyte saturated with O_2.

RDE allows the measurement of ORR and OER reactions. As two kinds of transitional metals were used to synthesise the catalyst, it is possible to analyze their influence on the electrochemical behaviour. In Figure 25 the justification for Co and Fe choice can be seen. Both reactions are compared to Pt-C. As can be noted, Fe increases the onset potential for both reactions, and Co increases the reaction rate and current density. However, only their combination results in the best outcome.

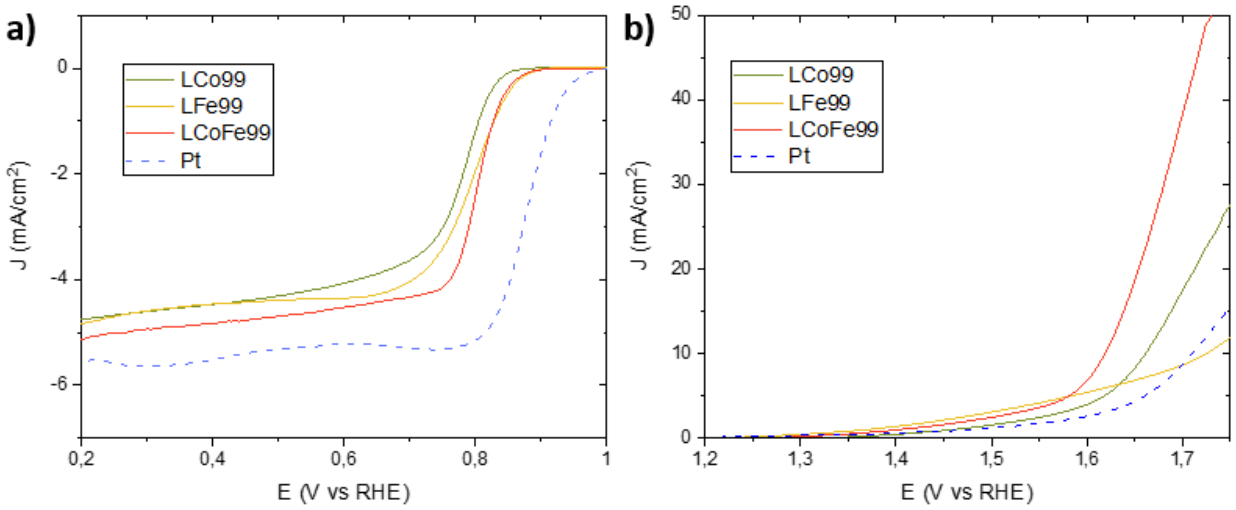

Figure 25 a) ORR and b) OER of samples with different metals 0.1 M KOH electrolyte saturated with O_2.

The choice of secondary carbonisation and its temperature can be investigated by the following ORR and OER plots (Figure 26 Figure 26). Secondary carbonisation slightly improves onset potential in the case of ORR. But only the second carbonisation at 900 °C provides improved current density. In the case of OER, the secondary carbonisation at 800 °C shifts the baseline closer to horizontal. But the OER current density is higher without the secondary carbonisation.

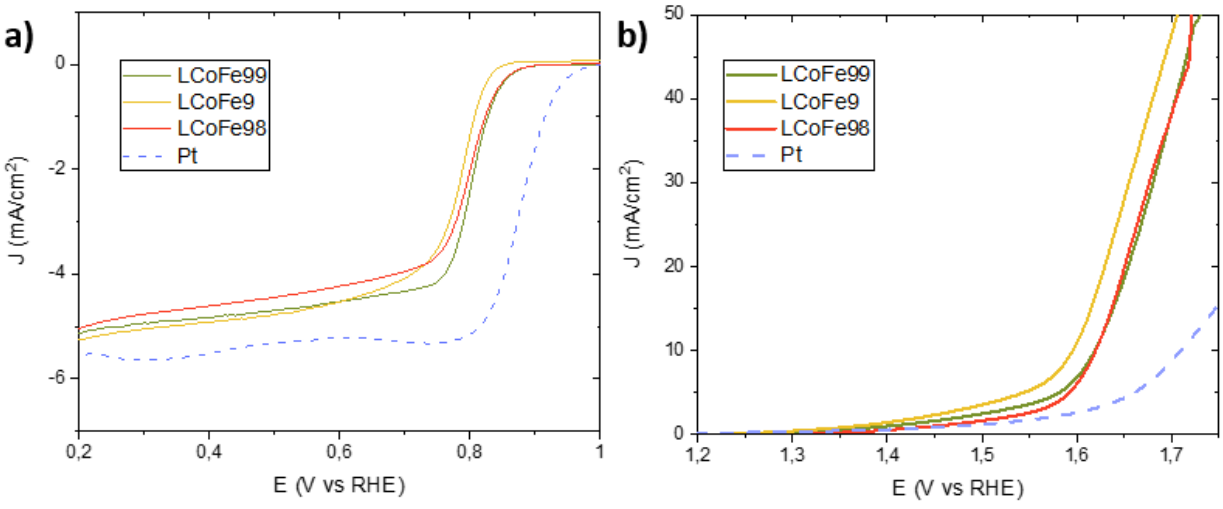

Figure 26 Effect of secondary pyrolysis on a) ORR and b) OER.

A decrease in double layer capacitance can also be seen on the CV after secondary carbonisation (see Figure 27). Nonetheless, the cathodic peak potential improves, as can be demonstrated by the CV plots. In the case of synthesised material, some OER properties can be sacrificed to improve ORR activity.

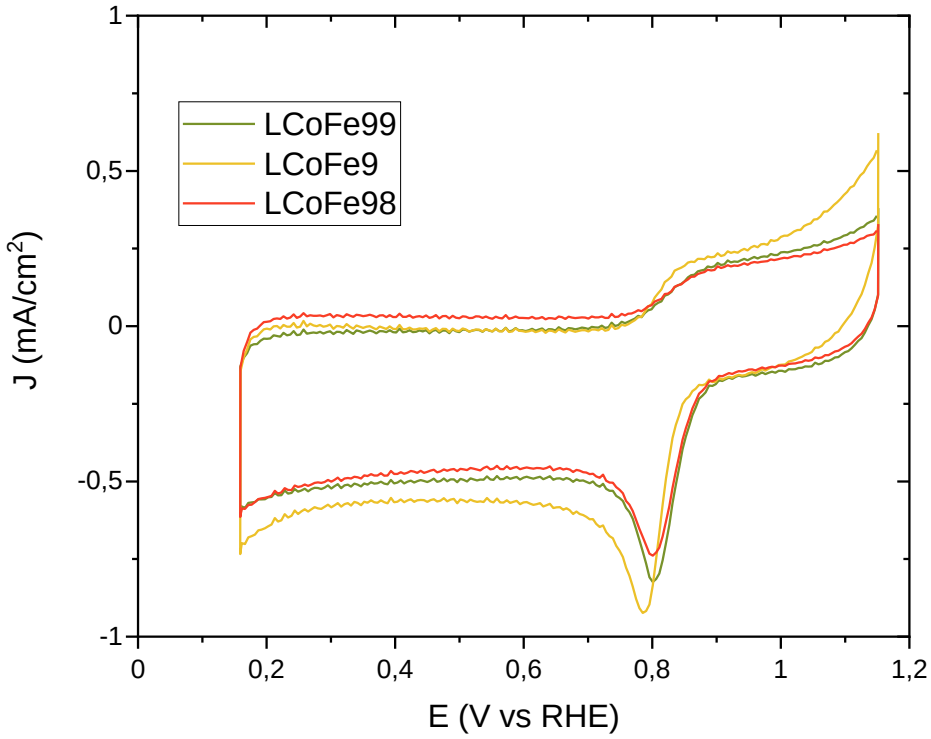

Figure 27 CV of samples with different secondary pyrolysis condition.

After these results were obtained, the best performing samples (i.e. synthesis conditions) were chosen for the rest of the study. For primary and secondary pyrolyses, the optimal temperature is 900 °C.

In an attempt to improve onset potential for both OER and ORR voltammograms, urea was added during synthesis to increase nitrogen content. Figure 28 shows the ORR and OER curves of the samples prepared by mixing bone and metals in one case, and with the addition of blood and urea before primary and secondary carbonisations.

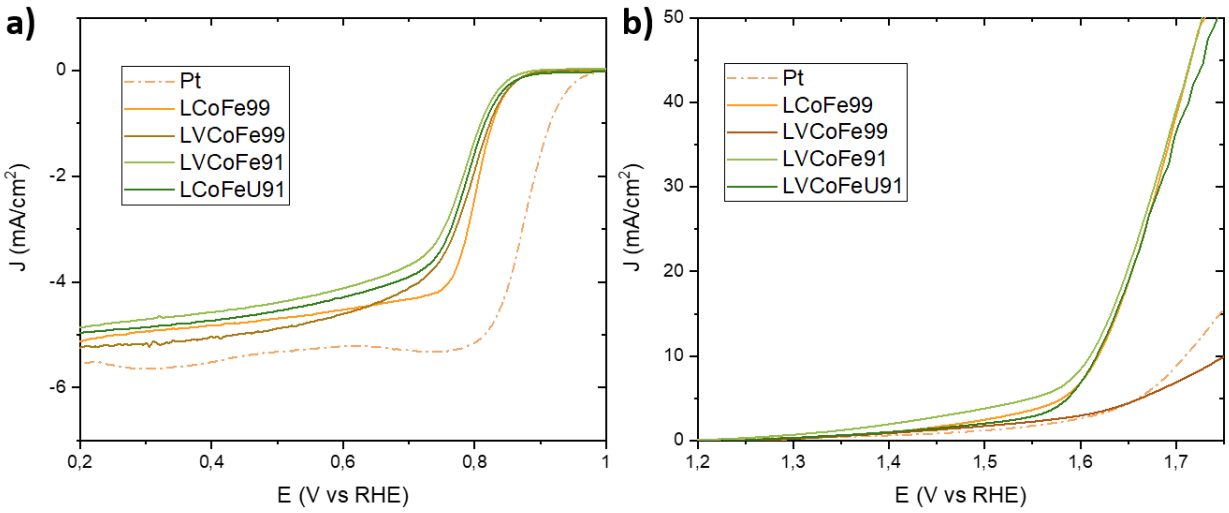

Figure 28 Effect of urea and blood and secondary pyrolysis temperature on a) ORR and b) OER.

It can be seen by onset potential in both reactions that the addition of urea did not show significant change in the electrocatalytic activity of the porous carbon. Moreover, the secondary carbonisation of 1000 °C reduced current density in the case of ORR. In OER the increased temperature of second carbonisation provoked the wide peak formation at the beginning of the reaction.

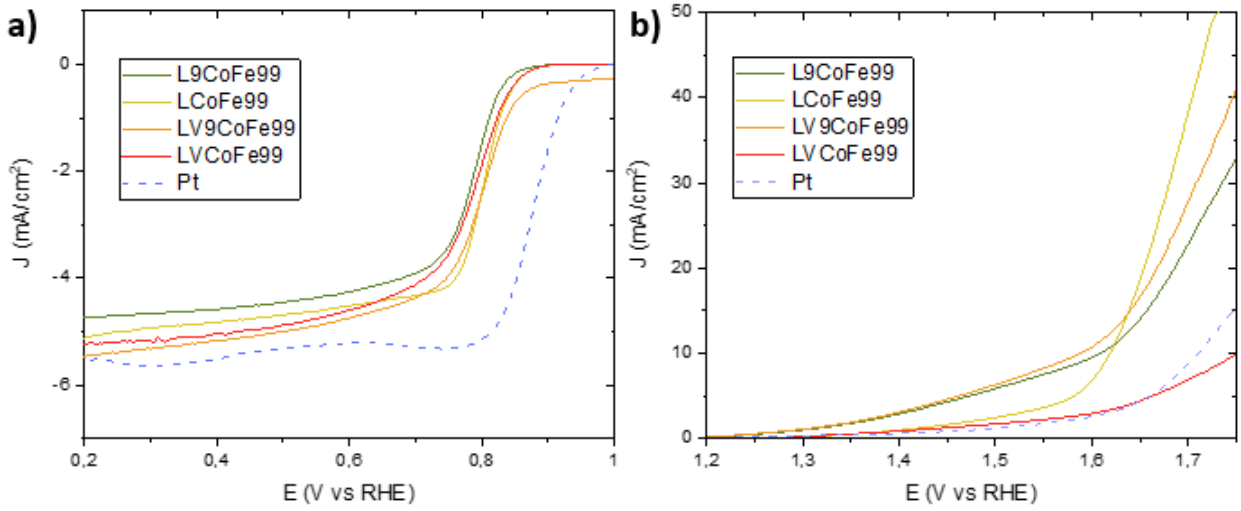

Figure 29 a) ORR and b) OER curves of the samples with different composition.

Figure 29 shows how ORR and OER plots can assist in the choice of the best composition for the porous doped carbon electrolyte. The following samples were compared: bone carbonised with metals (LCoFe99), bone and blood carbonised with metals (LVCoFe99), carbon produced from bone mixed with metals (L9CoFe99), and a bone and blood carbon mixed with metals (LV9CoFe99). The best performance in both reactions can be attributed to LCoFe99.

4.3. Overall performance

Chronoamperometry is used to test the stability of the catalysts at a constant potential and electrolyte flow. Figure 30 shows the relative current produced by catalysts over 20 h. The presence of Co indicates a significant improvement in stability, while a sample containing only Fe maintains only 50% stability. An increase in temperature of the secondary carbonisation to 1000 °C improves the stability of an electrolyte by 10%. Moreover, carbon mixed with metals showed better stability, rather the bone/blood/metal carbonised mixture. The instability of the catalyst may come mostly from the deterioration of the transitional metals. Another reason for the current decay may be due to the oxidation of the carbon.

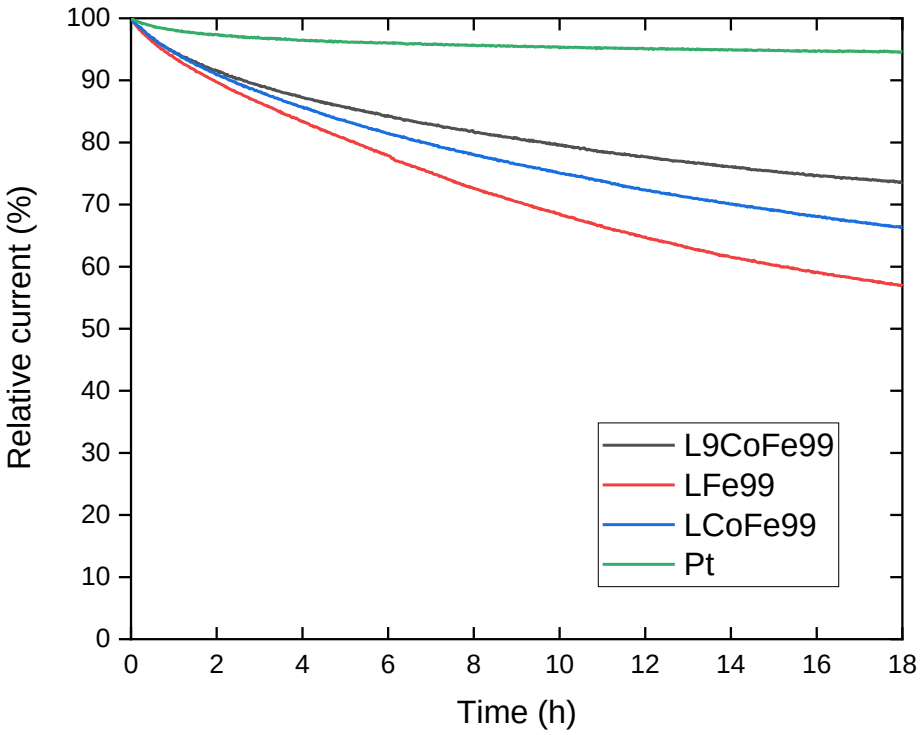

Figure 30 Chronoamperogram (stability test) of Pt-C, L9CoFe99, LCoFe99, LFe99, in 0.1 M KOH electrolyte, O_2 saturated.

Pt-C catalyst lost approximately 6% of its current over 17 h. This stability is significantly higher compared to some reported values of 65% (Dou et al., 2016). When such contradiction occurs, more attention has to be given to trustworthiness of both results and the reference material. Other research demonstrated higher Pt-C stability of about 80%, which is still lower than in the case of the synthesised materials (Jian Zhang et al., 2015b, Borghei et al., 2017). Increased stability can be a result of a better stability of the customized electrochemical ink.

The best performing samples (LCoFe99 and LCoFeU99) were chosen to be tested for stability in the GDE setup. Only a limited number of samples tested since all defining information about electrocatalytical behaviour can be obtained from RDE measurements.

Prior to stability measurements, CV and LSV tests were performed to establish the basic parameters of the catalyst in the new conditions. In Figure 31 a CV of both samples and an empty GDE are shown. An empty GDE CV was measured to eliminate the possibility of it interfering with the catalyst reaction. It can be seen that the extent of the CV for empty GDE

does not exceed the reaction of the catalyst. In this way the reliability of the results was also established.

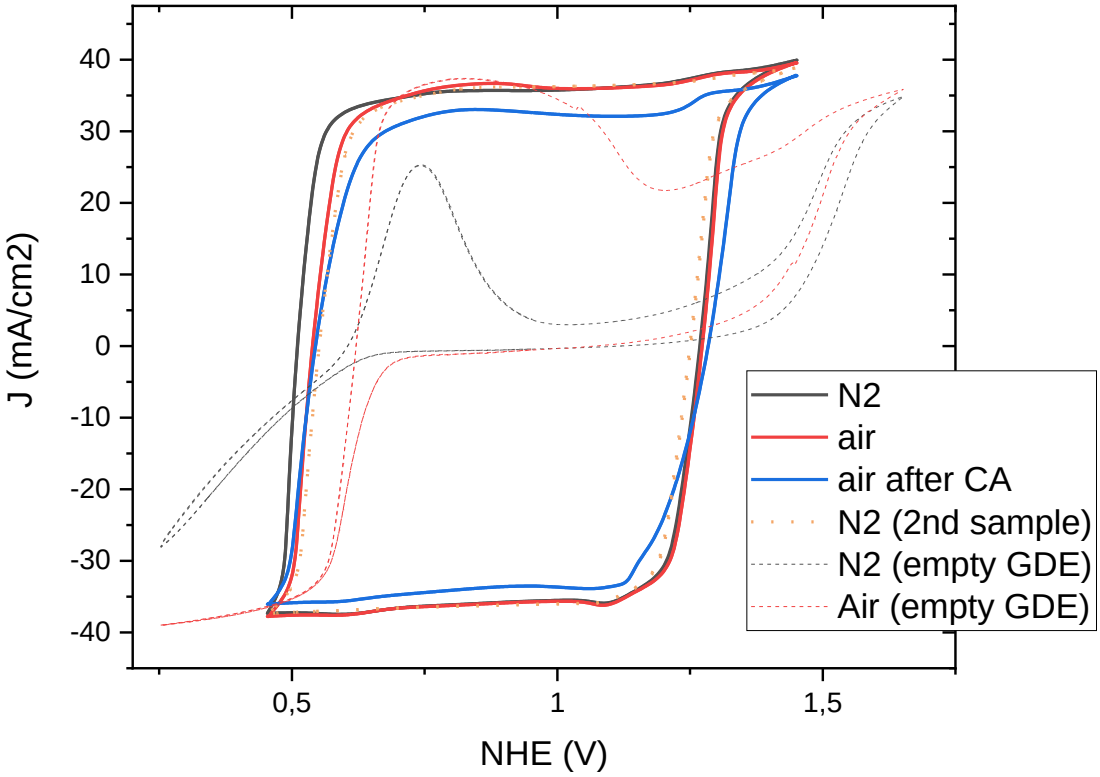

Figure 31 CV of LCoFe99 and empty GDE, 6 M KOH electrolyte, N_2 and synthetic air saturated.

Figure 32 demonstrates the ORR and OER behaviour of the porous carbon catalyst and the empty GDE. Once again, GDE does not show an interference with the catalyst reaction. The current density and speed of both reactions are much smaller for the GDE.

Meanwhile, both catalysts demonstrate similar ORR and OER behaviour to those observed by RDE. The current density is much higher due to a higher ion concentration in the electrolyte solution. Figure 32 shows that the sample without urea is more electrocatalytically active.

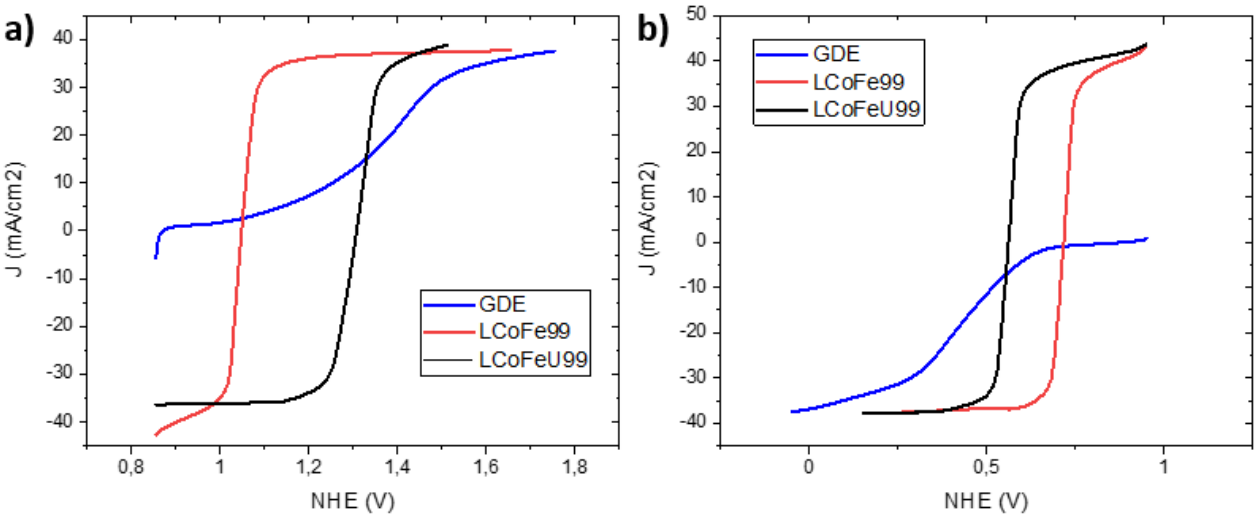

Figure 32 a) ORR and b) OER behaviour of LCoFe99 and LCoFeU99 in GDE tests, 6 M KOH electrolyte, N_2 saturated.

The stability measurement with the GDE took 17 h. The voltage was swept positively and negatively over this time. The extent of OER reaction in the positive current region is bigger than ORR in the negative region for both samples (see Figure 33). This outperformance is confirmation of the previous results.

Here the sample without urea shows better stability. In the beginning of the stability test the sample without urea distinctively outperforms in the ORR. However, by the end of the experiment the values are almost the same. Furthermore, if the second last cycle is noted, the current increases for ORR reaction. This change in current occurred when oxygen flow was restored. The length of the experiment was not conducive to constant supervision of the conditions, and the flow of the gas stopped at some point during the experiment. The insufficient access of oxygen resulted in a drop of current. Nevertheless, the activity of the catalyst did not drop according to the chronoamperogram.

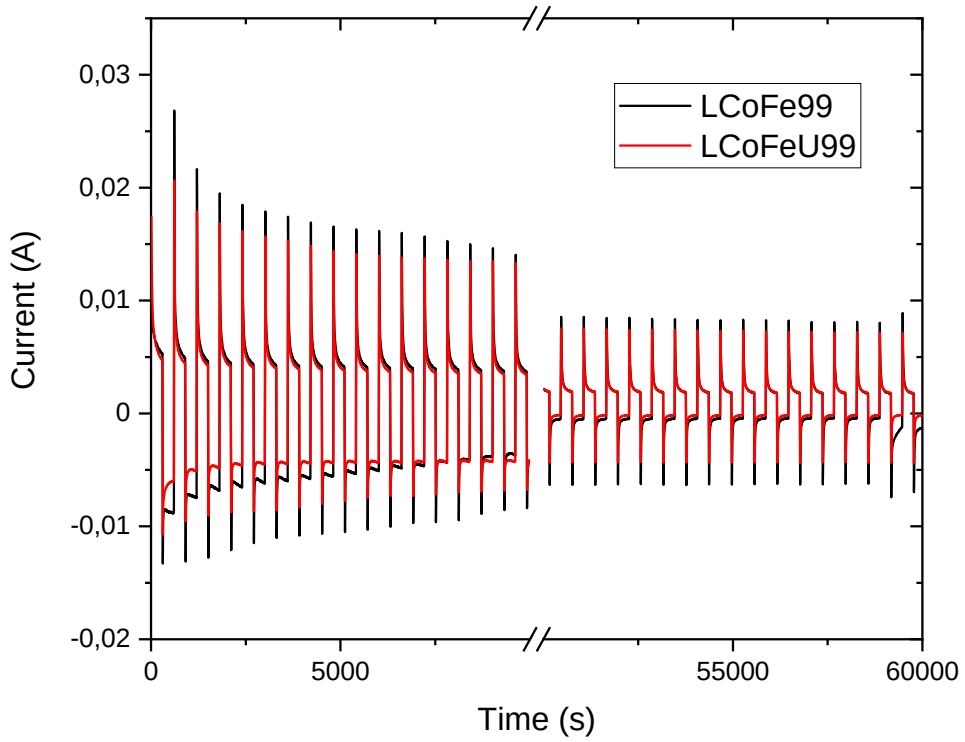

Figure 33 Charge-discharge cycles (stability test) of LCoFe99 and LCoFeU99 with GDE, in 6 M KOH electrolyte, synthetic air saturated.

5. Summary

This project's objectives were to develop bifunctional catalysts for the ORR and OER that occur at the cathode side of a metal-air battery. The catalyst was based on heteroatom doped porous carbon derived from biomass to promote sustainability. The catalyst was developed from waste and low-cost materials. Methods chosen for this work observed protocol for Health and Safety in the application of both materials and conditions.

As a result of the practical work, a promising catalyst was synthesised. The morphology and electroactivity of the catalyst were analysed. This allowed comparison with the commercial catalysts. Moreover, conclusions were made on the effects of synthesis parameters and precursors used on the carbon catalyst's performance.

Overall, the catalyst developed from animal bone materials with doping of cobalt and iron showed comparable ORR and OER activity. There are still ways that can result in improvement of the formulated catalyst.

Animal bone as a precursor material proved to be a favourable precursor for catalytic carbon. The preparation of carbon was executed through pyrolysis in a tube furnace at a heating rate of 5 °C/min to 900 °C and maintained for 2 h. The best electrocatalytically performing catalyst resulted from the carbonisation of a mixture of bone with iron and cobalt precursors followed by the acid wash and a second heat treatment at 900 °C.

Even though the electron configuration of a material depends on its structural properties, no significant effect of surface morphology on electrocatalytic properties was noted. SEM images could assist in the determination of general morphology and presence of doping.

Great attention was given to the preparation of the electrochemical ink in this research. Ideally, the composition of the conductive ink has to be developed for each catalyst individually. The same formulation was used for all catalysts in this research. The difference in the behaviour of the inks could be noted. Most importantly, the ink was optimised to produce a mechanically robust catalyst layer that withstands external loads and pressure from within the pores.

Electrochemical measurements were used to estimate the extent of ORR and OER. The porous carbon showed inferior ORR to the commercial catalyst (20% Pt on Vulcan, Pt-C). Nevertheless, the current density reached similar value as Pt-C, the onset potential yet requires to be improved further. Borghei et al. (2017) report the range of ORR onset potentials

achieved with similar catalysts. The onset potential for those would be 0.64 – 0.84 V vs NHE. While the best performing sample LCoFe99 reached only 0.82 V vs NHE onset potential. In the case of OER, the results were positive. The best performing ORR catalyst also performed best for the OER. It outperformed Pt-C, and optimisation techniques worked well.

Stability of the catalyst was measured over 17 – 20 h at the applied potential. The best current stability reached 70 %. Loss of metals might be the reason for the drop in performance. Stabilities dropped in the experiments with both configurations of RDE and GDE.

The limitation of this study was the short timeframe of the lab work. Some of the procedures in this work were performed or developed for the first time and required thorough research and development. For example, the work with potentiostat required the setting up of the equipment and methods. Furthermore, the conductive ink development took more time than was originally estimated at the outset due to the specificity of the materials used.

Overall, the extensive scope of information and practical experiments were covered in this project. In this way, many blind spots are still left within the project research. Additionally, suggestions for further research are recommended.

Morphology of the materials can be studied better to understand its relation to the electron transfer mechanism in the porous carbon. Likewise, more detailed information about the configuration and mechanism of attachment of the metals has to be obtained.

TEM images can provide more information on the interior structure of the carbon. However, the magnetism of the samples does not allow stabilisation of the electron beam on the surface. A special technique must be applied to obtain TEM images with the synthesised catalyst.

Improvement to the onset potential can be brought about with the addition of nitrogen. Nitrogen increases conductivity by lowering the bandgap for the system. During the project, urea was added as another nitrogen-containing precursor in an attempt to increase nitrogen content. However, it did not improve the electrocatalytic performance. The ability of urea to anchor to the compounds and alternative methods for nitrogen enrichments should be considered in the future. Also, other ways to improve onset potential must be analyzed.

New methods for doping should be tested to improve the stability of metals within the carbon structure. Stability tests showed degradation of the activity over time that can be attributed to the loss of the transitional metals or carbon support oxidation. This issue could benefit form more extensive research.

Also, an elemental composition of samples would help to reveal the amount of metals in different samples. Similarly, the carbon to nitrogen ratio determination is essential in this study.

The performance of the catalyst in the GDE is promising. Nonetheless, more experiments should be conducted with more attention to the preservation of constant gas flow conditions.

During the GDE measurements, the extensive capacity of the catalyst was noted. This led to new tests of the catalyst, which confirmed the ability of the material to function as a potential electrode for a supercapacitor. This research is currently ongoing in order to establish perspectives concerning the developed porous carbon, which might be employed in the area of energy storage devices.

References

4 Charts Explain Greenhouse Gas Emissions by Countries and Sectors | World Resources Institute. (n.d.). Retrieved January 7, 2021, from https://www.wri.org/blog/2020/02/greenhouse-gas-emissions-by-country-sector

Abnisa, F., Wan Daud, W. M. A., Ramalingam, S., Azemi, M. N. B. M., & Sahu, J. N. (2013). Co-pyrolysis of palm shell and polystyrene waste mixtures to synthesis liquid fuel. *Fuel*, *108*, 311–318. https://doi.org/10.1016/j.fuel.2013.02.013

Air Electrode Battery Market Size | Industry Report, 2020-2027. (n.d.). Retrieved October 18, 2020, from https://www.grandviewresearch.com/industry-analysis/air-electrode-battery-market

Alonso-Lemus, I. L., Figueroa-Torres, M. Z., Lardizabal-Gutíerrez, D., Bartolo-Pérez, P., Carrillo-Rodríguez, J. C., & Rodríguez-Varela, F. J. (2019). Converting chicken manure into highly active N-P co-doped metal-free biocarbon electrocatalysts: Effect of chemical treatment on their catalytic activity for the ORR. *Sustainable Energy and Fuels*, *3*(5), 1307–1316. https://doi.org/10.1039/c8se00583d

Asmadi, M., Kawamoto, H., & Saka, S. (2011). Gas- and solid/liquid-phase reactions during pyrolysis of softwood and hardwood lignins. *Journal of Analytical and Applied Pyrolysis*, *92*(2), 417–425. https://doi.org/10.1016/j.jaap.2011.08.003

Bai, X., Wang, G., Zhu, Z., Cai, C., Wang, Z., & Wang, D. (2020). Investigation of improving the yields and qualities of pyrolysis products with combination rod-milled and torrefaction pretreatment. *Renewable Energy*, *151*. https://doi.org/10.1016/j.renene.2019.11.040

Banham, D., Ye, S., Pei, K., Ozaki, J. I., Kishimoto, T., & Imashiro, Y. (2015). A review of the stability and durability of non-precious metal catalysts for the oxygen reduction reaction in proton exchange membrane fuel cells. In *Journal of Power Sources* (Vol. 285, pp. 334–348). Elsevier B.V. https://doi.org/10.1016/j.jpowsour.2015.03.047

Bard, A. J., Faulkner, L. R., & Wiley, J. (2001). *ELECTROCHEMICAL METHODS Fundamentals and Applications*.

Battery prices are falling, which is good news for EVs - Marketplace. (n.d.). Retrieved February 1, 2021, from https://www.marketplace.org/2019/12/03/battery-prices-falling-good-for-evs/

Borghei, M., Laocharoen, N., Kibena-Põldsepp, E., Johansson, L. S., Campbell, J., Kauppinen, E., Tammeveski, K., & Rojas, O. J. (2017). Porous N,P-doped carbon from coconut shells with high electrocatalytic activity for oxygen reduction: Alternative to Pt-C for alkaline fuel cells. *Applied Catalysis B: Environmental*, *204*, 394–402. https://doi.org/10.1016/j.apcatb.2016.11.029

Bridgwater, A. v. (2012). Review of fast pyrolysis of biomass and product upgrading. *Biomass and Bioenergy*, *38*, 68–94. https://doi.org/10.1016/j.biombioe.2011.01.048

Cazetta, A. L., Azevedo, S. P., Pezoti, O., Souza, L. S., Vargas, A. M. M., Paulino, A. T., Moraes, J. C. G., & Almeida, V. C. (2014). Thermally activated carbon from bovine bone: Optimization of synthesis conditions by response surface methodology. *Journal of Analytical and Applied Pyrolysis*, *110*(1), 455–462. https://doi.org/10.1016/j.jaap.2014.10.022

Couhert, C., Commandré, J. M., & Salvador, S. (2009). Failure of the component additivity rule to predict gas yields of biomass in flash pyrolysis at 950 °C. *Biomass and Bioenergy*, *33*(2). https://doi.org/10.1016/j.biombioe.2008.07.003

Couhert, C., Commandre, J. M., & Salvador, S. (2009). Is it possible to predict gas yields of any biomass after rapid pyrolysis at high temperature from its composition in cellulose, hemicellulose and lignin? *Fuel*, *88*(3). https://doi.org/10.1016/j.fuel.2008.09.019

Dennis, W. H. (2010). *Metallurgy: 1863-1963* (1st Editio). Routledge Book. https://www.routledge.com/Metallurgy-1863-1963/Dennis/p/book/9780202363615

Doktor, T., Valach, J., Kytýř, D., Jiroušek, O. (2011). Pore Size Distribution of Human Trabecular Bone - Comparison of Intrusion Measurements with Image Analysis. *Conference: Engineering Mechanics 2011*, *May*.

Dong, Q., & Wang, D. (2018). Catalysts in metal-air batteries. *MRS Communications*, *8*(2), 372–386. https://doi.org/10.1557/mrc.2018.59

Dou, M., He, D., Shao, W., Liu, H., Wang, F., & Dai, L. (2016). Pyrolysis of Animal Bones with Vitamin B12: A Facile Route to Efficient Transition Metal-Nitrogen-Carbon (TM-N-C) Electrocatalysts for Oxygen Reduction. *Chemistry - A European Journal*, *22*(9), 2896–2901. https://doi.org/10.1002/chem.201504983

Energy Investing Exploring Risk and Return in the Capital Markets - CCFI, IEA Report - v2 June 2020.pdf | Powered by Box. (n.d.). Retrieved January 7, 2021, from https://imperialcollegelondon.app.box.com/s/f1r832z4apqypw0fakk1k4ya5w30961g

Fanourgakis, G. S., Gkagkas, K., Tylianakis, E., & Froudakis, G. E. (2020). A Universal Machine Learning Algorithm for Large-Scale Screening of Materials. *Journal of the American Chemical Society*, *142*(8), 3814–3822. https://doi.org/10.1021/jacs.9b11084

Florencio-Silva, R., Sasso, G. R. D. S., Sasso-Cerri, E., Simões, M. J., & Cerri, P. S. (2015). Biology of Bone Tissue: Structure, Function, and Factors That Influence Bone Cells. In *BioMed Research International* (Vol. 2015). Hindawi Publishing Corporation. https://doi.org/10.1155/2015/421746

Fourmond, V., & Léger, C. (2019). An introduction to electrochemical methods for the functional analysis of metalloproteins. In *Practical Approaches to Biological Inorganic Chemistry* (pp. 325–373). Elsevier. https://doi.org/10.1016/B978-0-444-64225-7.00009-2

Franke-Whittle, I. H., & Insam, H. (2013). Treatment alternatives of slaughterhouse wastes, and their effect on the inactivation of different pathogens: A review. In *Critical Reviews in Microbiology* (Vol. 39, Issue 2, pp. 139–151). Taylor & Francis. https://doi.org/10.3109/1040841X.2012.694410

Guo, C., Hu, R., Liao, W., Li, Z., Sun, L., Shi, D., Li, Y., & Chen, C. (2017). Protein-enriched fish “biowaste” converted to three-dimensional porous carbon nano-network for advanced oxygen reduction electrocatalysis. *Electrochimica Acta*, *236*, 228–238. https://doi.org/10.1016/j.electacta.2017.03.169

Hartmann, P., Bender, C. L., Vračar, M., Dürr, A. K., Garsuch, A., Janek, J., & Adelhelm, P. (2013). A rechargeable room-temperature sodium superoxide (NaO2) battery. *Nature Materials*, *12*(3), 228–232. https://doi.org/10.1038/nmat3486

Hausker, K. (2019). *Zero-Net Emissions by 2050: Climate Realities and Challenges*. https://digitalcommons.wcupa.edu/srca_sp/5

Holy Grail. (n.d.). Retrieved January 18, 2021, from https://www.holygrail.ai/

Home | Métalectrique. (n.d.). Retrieved February 1, 2021, from https://www.metalectrique.com/

Hu, C., & Dai, L. (2017). Multifunctional Carbon-Based Metal-Free Electrocatalysts for Simultaneous Oxygen Reduction, Oxygen Evolution, and Hydrogen Evolution. *Advanced Materials*, *29*(9). https://doi.org/10.1002/adma.201604942

Hu, G., Li, J., Zhang, X., & Li, Y. (2017). Investigation of waste biomass co-pyrolysis with petroleum sludge using a response surface methodology. *Journal of Environmental Management*, *192*, 234–242. https://doi.org/10.1016/j.jenvman.2017.01.069

Hu, J., Jiang, B., Liu, J., Sun, Y., & Jiang, X. (2019). Influence of interactions between biomass components on physicochemical characteristics of char. *Journal of Analytical and Applied Pyrolysis*, *144*. https://doi.org/10.1016/j.jaap.2019.104704

Huang, W., Zhang, H., Huang, Y., Wang, W., & Wei, S. (2011). Hierarchical porous carbon obtained from animal bone and evaluation in electric double-layer capacitors. *Carbon*, *49*(3), 838–843. https://doi.org/10.1016/j.carbon.2010.10.025

Isahak, W. N. R. W., Hisham, M. W. M., Yarmo, M. A., & Yun Hin, T. Y. (2012). A review on bio-oil production from biomass by using pyrolysis method. In *Renewable and Sustainable Energy Reviews* (Vol. 16, Issue 8, pp. 5910–5923). https://doi.org/10.1016/j.rser.2012.05.039

Jaouen, F., Proietti, E., Lefèvre, M., Chenitz, R., Dodelet, J. P., Wu, G., Chung, H. T., Johnston, C. M., & Zelenay, P. (2011). Recent advances in non-precious metal catalysis for oxygen-reduction reaction in polymer electrolyte fuel cells. *Energy and Environmental Science*, *4*(1), 114–130. https://doi.org/10.1039/c0ee00011f

Jung, K. N., Lee, J. I., Jung, J. H., Shin, K. H., & Lee, J. W. (2014). A quasi-solid-state rechargeable lithium-oxygen battery based on a gel polymer electrolyte with an ionic liquid. *Chemical Communications*, *50*(41), 5458–5461. https://doi.org/10.1039/c4cc01243g

Just How Good An Investment Is Renewable Energy? New Study Reveals All. (n.d.). Retrieved January 7, 2021, from https://www.forbes.com/sites/davidrvetter/2020/05/28/just-how-good-an-investment-is-renewable-energy-new-study-reveals-all/?sh=3dadc1974d27

Kamat, A., Huth, A., Klein, O., Scholl, S., Kamat, A., Huth, A., Klein, O., & Scholl, S. (2010). *Chronoamperometric Investigations of the Electrode-Electrolyte Interface of a Commercial High Temperature PEM Fuel Cell . 6*, 10. https://doi.org/10.1002/fuce.201000014ï

Kang, B. K., Im, S. Y., Lee, J., Kwag, S. H., Kwon, S. bin, Tiruneh, S. N., Kim, M. J., Kim, J. H., Yang, W. S., Lim, B., & Yoon, D. H. (2019). In-situ formation of MOF derived mesoporous Co3N/amorphous N-doped carbon nanocubes as an efficient electrocatalytic oxygen evolution reaction. *Nano Research*, *12*(7), 1605–1611. https://doi.org/10.1007/s12274-019-2399-3

Koschwanez, H. E., & Reichert, W. M. (2013). Textured and Porous Materials. In *Biomaterials Science: An Introduction to Materials: Third Edition* (pp. 321–331). Elsevier Inc. https://doi.org/10.1016/B978-0-08-087780-8.00030-9

Krzesińska, M., & Majewska, J. (2015). Physical properties of continuous matrix of porous natural hydroxyapatite related to the pyrolysis temperature of animal bones precursors. *Journal of Analytical and Applied Pyrolysis*, *116*, 202–214. https://doi.org/10.1016/j.jaap.2015.09.009

Kumar, R., Varshney, S., Kar, K. K., & Dasgupta, K. (2019). Fabrication and characterisation of eco-friendly human-hair derived porous carbon-filled carbon fabric-reinforced polymer

composites. *Polymer Composites*, *40*(S2), E1573–E1587. https://doi.org/10.1002/pc.25078

Lao-atiman, W., Bumroongsil, K., Arpornwichanop, A., Bumroongsakulsawat, P., Olaru, S., & Kheawhom, S. (2019). Model-Based Analysis of an Integrated Zinc-Air Flow Battery/Zinc Electrolyzer System. *Frontiers in Energy Research*, *7*(FEB), 15. https://doi.org/10.3389/fenrg.2019.00015

Li, B. Q., Xia, Z. J., Zhang, B., Tang, C., Wang, H. F., & Zhang, Q. (2017). Regulating p-block metals in perovskite nanodots for efficient electrocatalytic water oxidation. *Nature Communications*, *8*(1), 1–7. https://doi.org/10.1038/s41467-017-01053-x

Li, M., Bi, X., Wang, R., Li, Y., Jiang, G., Li, L., Zhong, C., Chen, Z., & Lu, J. (2020). Relating Catalysis between Fuel Cell and Metal-Air Batteries. In *Matter* (Vol. 2, Issue 1, pp. 32–49). Cell Press. https://doi.org/10.1016/j.matt.2019.10.007

Liu, Q., Zhong, Z., Wang, S., & Luo, Z. (2011). Interactions of biomass components during pyrolysis: A TG-FTIR study. *Journal of Analytical and Applied Pyrolysis*, *90*(2), 213–218. https://doi.org/10.1016/j.jaap.2010.12.009

Liu, Xiaojun, Zhou, W., Yang, L., Li, L., Zhang, Z., Ke, Y., & Chen, S. (2015). Nitrogen and sulfur co-doped porous carbon derived from human hair as highly efficient metal-free electrocatalysts for hydrogen evolution reactions. *Journal of Materials Chemistry A*, *3*(16), 8840–8846. https://doi.org/10.1039/c5ta01209k

Liu, Xu, Wang, L., Yu, P., Tian, C., Sun, F., Ma, J., Li, W., & Fu, H. (2018). A Stable Bifunctional Catalyst for Rechargeable Zinc–Air Batteries: Iron–Cobalt Nanoparticles Embedded in a Nitrogen-Doped 3D Carbon Matrix. *Angewandte Chemie - International Edition*, *57*(49), 16166–16170. https://doi.org/10.1002/anie.201809009

Long, Y., Zhou, H., Meng, A., Li, Q., & Zhang, Y. (2016). Interactions among biomass components during co-pyrolysis in (macro)thermogravimetric analyzers. *Korean J. Chem. Eng*, *33*(9), 2638–2643. https://doi.org/10.1007/s11814-016-0102-x

Lv, X., Chen, Y., Wu, Y., Wang, H., Wang, X., Wei, C., Xiao, Z., Yang, G., & Jiang, J. (2019). A Br-regulated transition metal active-site anchoring and exposure strategy in biomass-derived carbon nanosheets for obtaining robust ORR/HER electrocatalysts at all pH values. *Journal of Materials Chemistry A*, *7*(47), 27089–27098. https://doi.org/10.1039/c9ta10880g

Ma, R., Lin, G., Zhou, Y., Liu, Q., Zhang, T., Shan, G., Yang, M., & Wang, J. (2019). A review of oxygen reduction mechanisms for metal-free carbon-based electrocatalysts. In *npj Computational Materials* (Vol. 5, Issue 1, pp. 1–15). Nature Publishing Group. https://doi.org/10.1038/s41524-019-0210-3

Martinez, U., Komini Babu, S., Holby, E. F., & Zelenay, P. (2018). Durability challenges and perspective in the development of PGM-free electrocatalysts for the oxygen reduction reaction. In *Current Opinion in Electrochemistry* (Vol. 9, pp. 224–232). Elsevier B.V. https://doi.org/10.1016/j.coelec.2018.04.010

Mastini, R., Kallis, G., & Hickel, J. (2021). A Green New Deal without growth? *Ecological Economics*, *179*, 106832. https://doi.org/10.1016/j.ecolecon.2020.106832

Niu, J., Shao, R., Liu, M., Zan, Y., Dou, M., Liu, J., Zhang, Z., Huang, Y., & Wang, F. (2019). Porous Carbons Derived from Collagen-Enriched Biomass: Tailored Design, Synthesis, and Application in Electrochemical Energy Storage and Conversion. *Advanced Functional Materials*, *29*(46), 1905095. https://doi.org/10.1002/adfm.201905095

Noh, W. Y., Lee, J. H., & Lee, J. S. (2020). Nitrogen-doped carbon nanotube–graphene hybrid stabilises MxN (M = Fe, Co) nanoparticles for efficient oxygen reduction reaction. *Applied Catalysis B: Environmental*, *268*, 118415. https://doi.org/10.1016/j.apcatb.2019.118415

Özkan, M., Borghei, M., Karakoç, A., Rojas, O. J., & Paltakari, J. (2018). Films based on cross-linked TEMPO-oxidised cellulose and predictive analysis via machine learning. *Scientific Reports*, *8*(1), 1–9. https://doi.org/10.1038/s41598-018-23114-x

Özkan, M., Karakoç, A., Borghei, M., Wiklund, J., Rojas, O. J., & Paltakari, J. (2019). Machine Learning assisted design of tailor-made nanocellulose films: A combination of experimental and computational studies. *Polymer Composites*, *40*(10), 4013–4022. https://doi.org/10.1002/pc.25262

Patel, S., Han, J., Qiu, W., & Gao, W. (2015). Synthesis and characterisation of mesoporous bone char obtained by pyrolysis of animal bones, for environmental application. *Journal of Environmental Chemical Engineering*, *3*(4), 2368–2377. https://doi.org/10.1016/j.jece.2015.07.031

Proano-Aviles, J. (2020). Opportunities to Enhance the Pyrolysis of Biomass in The Production of Hydroxyapatite and Chemicals. *American Journal of Biomedical Science & Research*, *8*(5), 438–442. https://doi.org/10.34297/ajbsr.2020.08.001315

Rafiq, S., Fu, B., Kudisch, B., & Scholes, G. D. (2020). Interplay of vibrational wavepackets during an ultrafast electron transfer reaction. *Nature Chemistry*. https://doi.org/10.1038/s41557-020-00607-9

Ren, M., Zhang, J., Zhang, C., Stanford, M. G., Chyan, Y., Yao, Y., & Tour, J. M. (2020). Quasi-Solid-State Li-O2 Batteries with Laser-Induced Graphene Cathode Catalysts. *ACS Applied Energy Materials*, *3*(2), 1702–1709. https://doi.org/10.1021/acsaem.9b02182

Samanya, J., Hornung, A., Apfelbacher, A., & Vale, P. (2012). Characteristics of the upper phase of bio-oil obtained from co-pyrolysis of sewage sludge with wood, rapeseed and straw. *Journal of Analytical and Applied Pyrolysis*, *94*, 120–125. https://doi.org/10.1016/j.jaap.2011.11.017

Sambudi, N. S., Cho, S., & Cho, K. (2016). Porous hollow hydroxyapatite microspheres synthesised by spray pyrolysis using a microalga template: Preparation, drug delivery, and bioactivity. *RSC Advances*, *6*(49), 43041–43048. https://doi.org/10.1039/c6ra03147a

Shao, Y., Dodelet, J. P., Wu, G., & Zelenay, P. (2019). PGM-Free Cathode Catalysts for PEM Fuel Cells: A Mini-Review on Stability Challenges. In *Advanced Materials* (Vol. 31, Issue 31). Wiley-VCH Verlag. https://doi.org/10.1002/adma.201807615

Singh, H., Zhuang, S., Ingis, B., Nunna, B. B., & Lee, E. S. (2019). Carbon-based catalysts for oxygen reduction reaction: A review on degradation mechanisms. In *Carbon* (Vol. 151, pp. 160–174). Elsevier Ltd. https://doi.org/10.1016/j.carbon.2019.05.075

Song, F., Li, W., Yang, J., Han, G., Yan, T., Liu, X., Rao, Y., Liao, P., Cao, Z., & Sun, Y. (2019). Interfacial sites between cobalt nitride and cobalt act as bifunctional catalysts for hydrogen electrochemistry. *ACS Energy Letters*, *4*(7), 1594–1601. https://doi.org/10.1021/acsenergylett.9b00738

Song, H., Li, H., Wang, H., Key, J., Ji, S., Mao, X., & Wang, R. (2014). Chicken bone-derived N-doped porous carbon materials as an oxygen reduction electrocatalyst. *Electrochimica Acta*, *147*, 520–526. https://doi.org/10.1016/j.electacta.2014.09.146

Strandberg, A., Holmgren, P., Wagner, D. R., Molinder, R., Wiinikka, H., Umeki, K., & Broström, M. (2017). Effects of Pyrolysis Conditions and Ash Formation on Gasification Rates of Biomass Char. *Energy and Fuels*, *31*(6), 6507–6514. https://doi.org/10.1021/acs.energyfuels.7b00688

Strelko, V. v., Kuts, V. S., & Thrower, P. A. (2000). On the mechanism of possible influence of heteroatoms of nitrogen, boron and phosphorus in a carbon matrix on the catalytic activity of carbons in electron transfer reactions. In *Carbon* (Vol. 38, Issue 10, pp. 1499–1503). https://doi.org/10.1016/S0008-6223(00)00121-4

Tao, L., Wang, Y., Zou, Y., Zhang, N., Zhang, Y., Wu, Y., Wang, Y., Chen, R., & Wang, S. (2020). Charge Transfer Modulated Activity of Carbon-Based Electrocatalysts. In *Advanced Energy Materials* (Vol. 10, Issue 11). Wiley-VCH Verlag. https://doi.org/10.1002/aenm.201901227

Tolera, S. T., & Alemu, F. K. (2020). Potential of Abattoir Waste for Bioenergy as Sustainable Management, Eastern Ethiopia, 2019. *Journal of Energy*, *2020*, 1–9. https://doi.org/10.1155/2020/6761328

Wang, H. F., Tang, C., & Zhang, Q. (2018). A Review of Precious-Metal-Free Bifunctional Oxygen Electrocatalysts: Rational Design and Applications in Zn–Air Batteries. In *Advanced Functional Materials* (Vol. 28, Issue 46). Wiley-VCH Verlag. https://doi.org/10.1002/adfm.201803329

Wang, H., Wang, K., Song, H., Li, H., Ji, S., Wang, Z., Li, S., & Wang, R. (2015). N-doped porous carbon material made from fish-bones and its highly electrocatalytic performance in the oxygen reduction reaction. *RSC Advances*, *5*(60), 48965–48970. https://doi.org/10.1039/c5ra09144f

Wang, R., Wang, K., Wang, Z., Song, H., Wang, H., & Ji, S. (2015). Pig bones derived N-doped carbon with multi-level pores as electrocatalyst for oxygen reduction. *Journal of Power Sources*, *297*, 295–301. https://doi.org/10.1016/j.jpowsour.2015.07.107

Wang, S., Jiang, X. M., Han, X. X., & Wang, H. (2008). Fusion characteristic study on seaweed biomass ash. *Energy and Fuels*, *22*(4), 2229–2235. https://doi.org/10.1021/ef800128k

Weeks, M. E. (1932). The discovery of the elements. III. some eighteenth-century metals. *Journal of Chemical Education*, *9*(PART I), 22–30. https://doi.org/10.1021/ed009p22

Wippert, P. M., Rector, M., Kuhn, G., & Wuertz-Kozak, K. (2017). Stress and alterations in bones: An interdisciplinary perspective. *Frontiers in Endocrinology*, *8*(MAY), 96. https://doi.org/10.3389/fendo.2017.00096

Xue, J., Ceylan, S., & Goldfarb, J. L. (2015). Synergism among biomass building blocks? Evolved gas and kinetics analysis of starch and cellulose co-pyrolysis. *Thermochimica Acta*, *618*, 36–47. https://doi.org/10.1016/j.tca.2015.09.002

Yan, H., Xie, Y., Wu, A., Cai, Z., Wang, L., Tian, C., Zhang, X., & Fu, H. (2019). Anion-Modulated HER and OER Activities of 3D Ni–V-Based Interstitial Compound Heterojunctions for High-Efficiency and Stable Overall Water Splitting. *Advanced Materials*, *31*(23). https://doi.org/10.1002/adma.201901174

Yildiz, G., Ronsse, F., Venderbosch, R., Duren, R. van, Kersten, S. R. A., & Prins, W. (2015). Effect of biomass ash in catalytic fast pyrolysis of pine wood. *Applied Catalysis B: Environmental*, *168–169*, 203–211. https://doi.org/10.1016/j.apcatb.2014.12.044

Yu, P., Wang, L., Sun, F., Xie, Y., Liu, X., Ma, J., Wang, X., Tian, C., Li, J., & Fu, H. (2019). Co Nanoislands Rooted on Co–N–C Nanosheets as Efficient Oxygen Electrocatalyst for Zn–Air Batteries. *Advanced Materials*, *31*(30), 1901666. https://doi.org/10.1002/adma.201901666

Zhang, Jian, Li, Q., Zhang, C., Mai, L., Pan, M., & Mu, S. (2015a). A N-self-doped carbon catalyst derived from pig blood for oxygen reduction with high activity and stability. *Electrochimica Acta*, *160*, 139–144. https://doi.org/10.1016/j.electacta.2015.01.200

Zhang, Jian, Li, Q., Zhang, C., Mai, L., Pan, M., & Mu, S. (2015b). A N-self-doped carbon catalyst derived from pig blood for oxygen reduction with high activity and stability. *Electrochimica Acta*, *160*, 139–144. https://doi.org/10.1016/j.electacta.2015.01.200

Zhang, Jie, Zhou, Q., Tang, Y., Zhang, L., & Li, Y. (2019). Zinc-air batteries: Are they ready for prime time? *Chemical Science*, *10*(39), 8924–8929. https://doi.org/10.1039/c9sc04221k

Zhang, M., Jin, X., Wang, L., Sun, M., Tang, Y., Chen, Y., Sun, Y., Yang, X., & Wan, P. (2017). Improving biomass-derived carbon by activation with nitrogen and cobalt for supercapacitors and oxygen reduction reaction. *Applied Surface Science*, *411*, 251–260. https://doi.org/10.1016/j.apsusc.2017.03.097

Zhang, X., Wang, X.-G., Xie, Z., & Zhou, Z. (2016). *Recent progress in rechargeable alkali metaleair batteries-NC-ND license (http://creativecommons.org/licenses/by-nc-nd/4.0/)*. https://doi.org/10.1016/j.gee.2016.04.004

Zhang, Z., Yang, S., Li, H., Zan, Y., Li, X., Zhu, Y., Dou, M., & Wang, F. (2019). Sustainable Carbonaceous Materials Derived from Biomass as Metal-Free Electrocatalysts. *Advanced Materials*, *31*(13), 1805718. https://doi.org/10.1002/adma.201805718

Zhao, S., Liu, M., Zhao, L., & Zhu, L. (2018). Influence of Interactions among Three Biomass Components on the Pyrolysis Behaviour. *Industrial and Engineering Chemistry Research*, *57*(15). https://doi.org/10.1021/acs.iecr.8b00593

Zhao, Z., Cannon, F. S., & Nieto-Delgado, C. (2019). Synergistic interaction between lignin and collagen during co-pyrolysis. *Carbon*, *154*, 254–265. https://doi.org/10.1016/j.carbon.2019.08.011

Zong, P., Jiang, Y., Tian, Y., Li, J., Yuan, M., Ji, Y., Chen, M., Li, D., & Qiao, Y. (2020). Pyrolysis behaviour and product distributions of biomass six group components: Starch, cellulose, hemicellulose, lignin, protein and oil. *Energy Conversion and Management*, *216*, 112777. https://doi.org/10.1016/j.enconman.2020.112777

Zou, H., Li, G., Duan, L., Kou, Z., & Wang, J. (2019). In situ coupled amorphous cobalt nitride with nitrogen-doped graphene aerogel as a trifunctional electrocatalyst towards Zn-air battery deriven full water splitting. *Applied Catalysis B: Environmental*, *259*, 118100. https://doi.org/10.1016/j.apcatb.2019.118100

Appendix

A. Cobalt

In culture Cobalt is traced back to 3000 BC but was discovered only in 1735 by Swedish chemist Georg Brandt. (Weeks, 1932)

The name cobalt is derived from German kobold (troll). It comes from miners' experience with the toxic odour and inability to smelt the ore, that would turn into cobalt oxide. (Dennis, 2010)

As the colour of cobalt adored by everybody, the production of dyes starts in Norway. But with discovery of cobalt belt in Congo in the beginning of 20th century, the biggest extraction takes place there until now.

Cobalt is an inorganic crystalline solid. cobalt anhydrite is in a lattice, resulting the blue colour. When cobalt is hydrated, the colour turns pink due to dissociation of ions. The picture demonstrates the solution of $CoCl_2$ and the dried mixture of bone and cobalt. The dehydration was successful!

B. TEM images

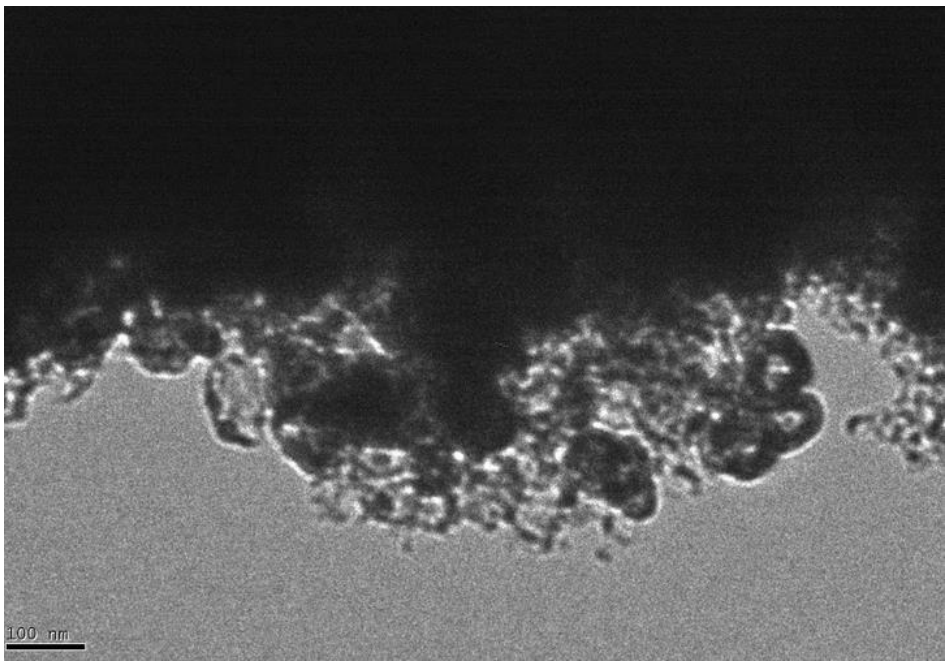

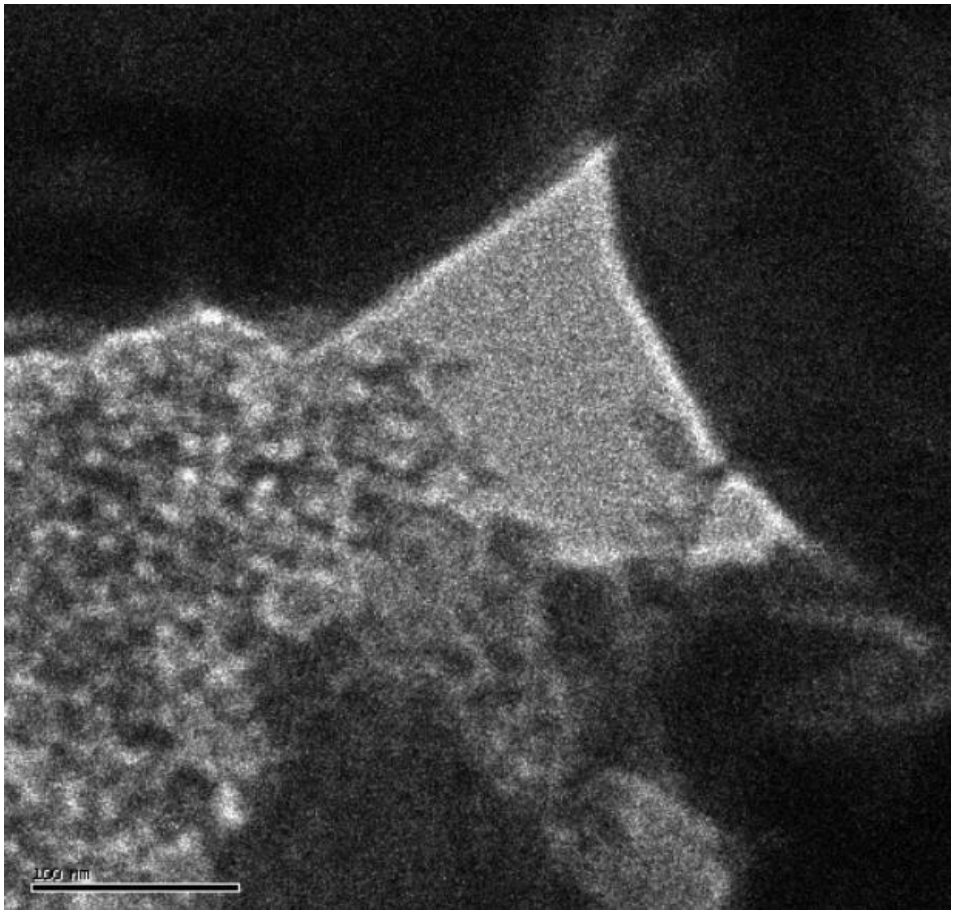

C. SEM image

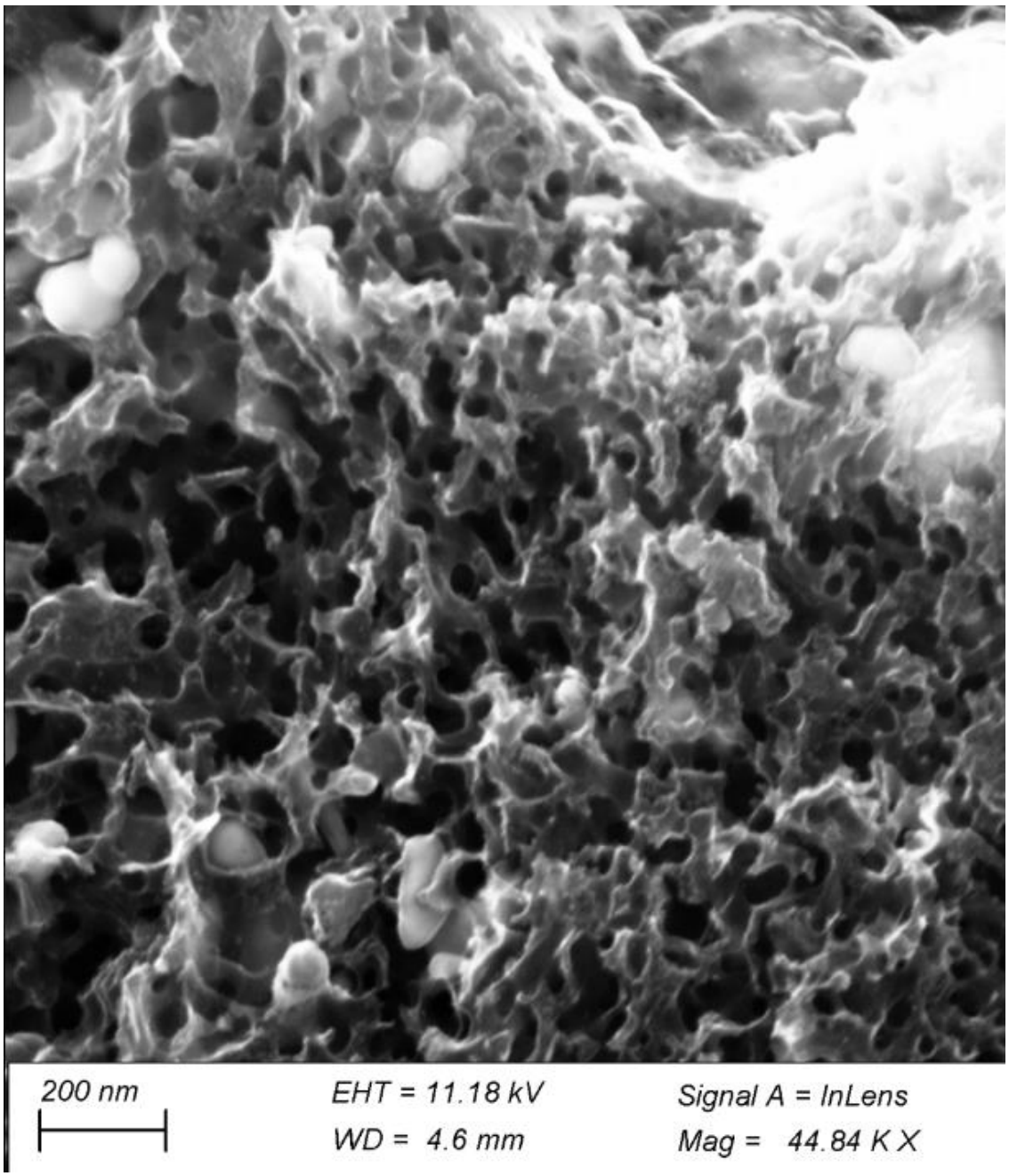

D. Protocol for glassy carbon electrode measurements

Electrode	Method	Gas	Computation	Range, V	Sweep rate, mV/s	Electrode range	Number of cycles
1	CV	Ar	iR off	0.2 - -0.8	50	10	26
	EIS-RU	Ar					
	CV	Ar	iR on	0.2 - -0.8	50	10	3
	LSV-ORR (1600 rpm)	Ar	iR on	0.2 - -0.8	50	20	1
	CV	Ar	iR on	0.2 - -0.8	50	10	3
	EIS-RU	O2					
	CV	O2	iR on	0.2 - -0.8	50	10	3
	RDE (400 rpm)	O2	iR on	0.2 - -0.8	50	20	1
	RDE (900 rpm)	O2	iR on	0.2 - -0.8	50	20	1
	RDE (1600 rpm)	O2	iR on	0.2 - -0.8	50	20	1
	RDE (2500 rpm)	O2	iR on	0.2 - -0.8	50	20	1
	RDE (3600 rpm)	O2	iR on	0.2 - -0.8	50	20	1
	CV	O2	iR on	0.2 - -0.8	50	10	3
	CA	O2	iR on	0 - 20 h			
2	CV	Ar	iR off	0.2 - -0.8	50	10	26
	EIS-RU	Ar					
	CV	Ar	iR on	0.2 - -0.8	50	10	3
	LSV-OER (1600 rpm)	Ar	iR on	0 - 1	50	20	1
	CV	Ar	iR on	0.2 - -0.8	50	10	3

E. Protocol for gas diffusion electrode measurements

Electrode	Method	Gas	Range	Sweep rate, mV/s	Electrode range, mA	Number of cycles
1	EIS-RU	N2	100 kHz - 100 mHz			
	CV	N2	0.5 - -0.5 V	50	10	15
	LSV-ORR (1600 rpm)	N2				
	EIS-RU	Air	100 kHz - 100 mHz			
	CV	Air	0.5 - -0.5 V	50	10	15
	CA	Air	0.34 - -0.45 V			
	EIS-RU	N2	100 kHz - 100 mHz			
	CV	N2	0.5 - -0.5 V	50	10	15
2	EIS-RU	N2	100 kHz - 100 mHz			
	CV	N2	0.5 - -0.5 V	50	10	15
	LSV-OER (1600 rpm)	N2				